Human TRMT2A methylates different components of the translation machinery and contributes to translation fidelity

Monika Witzenberger[1], Sandra Burczyk[2], Luisa M. Welp[3], Mirko Wagner[5], Thomas Monecke[2], Robert Janowski[1], Thomas Carell[5], Henning Urlaub[3,4], Stefanie M. Hauck[6], Aaron Voigt[7,*], Dierk Niessing[1,*]

1 Institute of Structural Biology, Helmholtz Zentrum München - German Research Center for Environmental Health, Neuherberg, Germany.
2 Institute of Pharmaceutical Biotechnology, Ulm University, Ulm, Germany.
3 Bioanalytical Mass Spectrometry Group, Max Planck Institute for Multidisciplinary Sciences, Göttingen, Germany.
4 Institute of Clinical Chemistry, University Medical Center Göttingen, Göttingen, Germany.
5 Department of Chemistry and Biochemistry, Ludwig-Maximilians University Munich, München, Germany.
6 Metabolomics and Proteomics CoreResearch Unit Protein Science, Helmholtz Zentrum München - German Research Center for Environmental Health, Neuherberg, Germany.
7 Department of Neurology, Faculty of Medicine, RWTH Aachen, Aachen, Germany.
* Correspondence should be addressed to:
Aaron Voigt (avoigt@ukaachen.de), Dierk Niessing (niessing@helmholtz-muenchen.de)

Abstract

Methyl-5-uridine (m5U) is one of the most abundant RNA modifications found in cytosolic tRNA. tRNA methyltransferase 2 homolog A (hTRMT2A) is the dedicated mammalian enzyme of m5U conversion at tRNA position 54. However, its RNA binding specificity and functional role in the cell are not well understood. Here we dissected structural and sequence requirements for binding and methylation of its RNA targets. Specificity of tRNA modification by TRMT2A is achieved by a combination of modest binding preference and presence of a uridine in position 54 of tRNAs. Mutational analysis together with crosslinking experiments identified a large hTRMT2A-tRNA binding surface. Furthermore, complementing hTRMT2A interactome studies revealed that TRMT2A interacts with proteins involved in both tRNA and rRNA biogenesis. Consistent with this finding, we observed that TRMT2A not only methylates tRNA, but also rRNA. Finally, we addressed the question of the importance of TRMT2A function by showing that its knockdown reduces translational fidelity. These findings extend the role of hTRMT2A beyond tRNA modification towards rRNA biogenesis and translational fidelity.

Introduction

Up to date more than 170 post-transcriptional modification were reported. They canPost-affect RNA stability, translation, and localization and, hence, constitute an important layer of gene regulation (Roundtree et al., 2017; Boo and Kim, 2020; Das et al., 2021). Amongst the different types of transcripts, tRNA is the most heavily modified RNA species with an average of 13 modifications per tRNA molecule (Boccaletto et al., 2018; Pan, 2018; Suzuki, 2021). These modifications play a role in tRNA stability and folding, although their exact biological function often remains elusive. The modification 5-methyluridine (m^5U) frequently occurs at position 54 in the T-Loop of bacterial and eukaryotic tRNAs (Boccaletto et al., 2018). While in *E. coli* the tRNA (uracil-C(5))-methyltransferase A (TrmA) is responsible for m^5U conversion, the respective homolog in *S. cerevisiae* is termed Trm2, and in mammals tRNA (uracil-5)-methyltransferase homolog A (TRMT2A) (Ny and Björk, 1980; Nordlund et al., 2000; Carter et al., 2019). In addition, mammals possess TRMTB, the mitochondria-specific paralog (Laptev et al., 2020; Powell and Minczuk, 2020).

Removal of the catalytic activity of TrmA does not impact the viability of *E. coli*, although deletion of the whole gene is lethal (Persson et al., 1992). In contrast, in budding yeast Trm2 is not essential for survival (Nordlund et al., 2000). Hence, these phenotypes suggest a supporting role of the enzyme in tRNA maturation and other yet unknown biological processes beyond m^5U catalysis (Johansson and Byström, 2002). For instance, *E. coli* TrmA has recently been reported to be a tRNA chaperone assisting proper tRNA folding (Keffer-Wilkes et al., 2020). Moreover, TrmA methylates not only tRNA, but also the T-Loop of tmRNA (Ranaei-Siadat et al., 2013) and 16S rRNA *in vitro* (Gustafsson and Björk, 1993).

Detailed biochemical and structural studies on *E. coli* TrmA have contributed to a better understanding of the general enzymatic mechanism for m^5U conversion. Most methyltransferases, including TrmA as well as human TRMT2A, use SAM (S-adenosyl-methionine) as methyl donor (Urbonavičius et al., 2007; Carter et al., 2019; Powell and Minczuk, 2020). Previous mutational studies identified catalytically relevant residues in TrmA. Enzymatic activity as well as RNA binding was reduced upon mutation of the catalytic cysteine (C324A).The putative SAM binding site (G220D), the proton abstraction base for the catalytic reaction (E358K) and one of the residues interacting with target uridine (Q190A) were important for RNA binding too (Urbonavičius et al., 2007). Furthermore, residues (H125A, F106) reduced tRNA binding and methylation, since they disrupt the tertiary interaction of T- and D-Loop (Keffer-Wilkes et al., 2020). Such biochemical studies were supported by a co-crystal structure of TrmA with the T-Loop of tRNA (Alian et al., 2008), confirming that the conserved C324 covalently binds to the target uridine, thus driving m^5U conversion.

Only very recently our knowledge about m^5U tRNA methyltransferases was expanded to human TRMT2A (hTRMT2A). Transcriptome-wide mapping of hTRMT2A methylation sites on

RNA using FICC-CLIP have revealed that 87% of the cellular hTRMT2A targets are indeed tRNAs (Carter et al., 2019). Binding sequences with the motif CTTCG/AA were enriched, which constitutes a conserved tRNA T-Loop sequence. However, hTRMT2A binding expands beyond tRNAs as observed by its interaction with the HIST1H4B or KCND2 mRNA, small subunit rRNA and other RNAs (Cheng et al., 2020; Dai et al., 2021). In line with such a broader function, its mammalian paralog TRMT2B was not only shown to be the dedicated mitochondrial methyltransferase for m^5U54 conversion in mitochondrial tRNAs, but also to promote m^5U429 conversion of mitochondrial 12S rRNA (Laptev et al., 2020; Powell and Minczuk, 2020). It remains to be shown whether also TRMT2A has a dual function on tRNA and rRNA.

The cellular role of hTRMT2A, m^5U conversion and possible roles beyond m^5U conversion are not well understood, although some functional observations have been made: while in one study, hTRMT2A overexpression correlated with Her^+ positive cancer (Hicks et al., 2010), in another study hTRMT2A was described as cell cycle regulator that suppresses cell proliferation (Chang et al., 2018). In a third study, hTRMT2A KO caused accumulation of tRNA-derived fragments (Pereira et al., 2021). Although the TRMT2A-bound RNAs have been identified (Carter et al. 2019), we lack an understanding of its protein interactome and hence an overview of the molecular pathways it contributes to. Furthermore, to date all molecular features of hTRMT2A have been inferred from orthologs in single-cell organisms.

In this study, we systematically characterized the functional and molecular features of hTRMT2A. Moreover, we identified hTRMT2A's determinants of specificity. We observed that hTRMT2A has only a modest binding preference for its physiological targets and that target specificity is rather achieved by the requirement of a uridine in the correct steric position to allow for site-specific methylation. Assessment of the cellular human TRMT2A interactome allowed us to identify potential co-factors, suggesting novel roles of hTRMT2A in different cellular processes. Moreover, we observed that hTRMT2A is required not only for tRNA but also for rRNA methylation. Finally, we show that loss of hTRMT2A in a cellular context resulted in reduced translation fidelity.

Materials and Methods

Cloning, expression in *E. coli* and purification. Plasmid containing human TRMT2A sequence was provided by Aaron Voigt. Human TRMT2A RBD (aa 69 – 147), central domain (aa 237-414) and fusion domain (aa 68-240/413-590) were cloned with a cleavable SUMO-tag at the N-terminus and expressed in Rosetta 2 (DE3) in case of RBD or Rosetta 2 (DE3) pLyS (Central, Fusion) *E. coli* in LB medium. After isopropyl-thiogalactoside (IPTG, 0.5 mM) induction over night at 18 °C, cells were harvested (4500 x *g*, 15 min, 4 °C). All purification steps were performed at 4 °C. For hTRMT2A RBD purification typically pellets from 6 liters of culture were resuspended in lysis buffer-A (50 mM HEPES-NaOH pH 8.5, 500 mM NaCl, 20 mM Imidazole, 0.5 % (v/v) Tween, 2 % Glycerol) supplemented with one tablet of EDTA-free protease inhibitor cocktail (Roche). After sonication (4x 6 min, amplitude 40 %, output: 6), the lysate was clarified by centrifugation (40,000 x *g*, 30 min). The lysate was loaded onto a 5 ml HisTrap FF column (GE Healthcare), equilibrated in His-A buffer (50 mM HEPES-NaOH pH 8.5, 500 mM NaCl, 20 mM Imidazole), and washed with 10 column volumes (CV) of His-A buffer, followed by a 10 CV wash with His-B buffer (50 mM HEPES-NaOH pH 8.5, 2000 mM NaCl, 20 mM Imidazole). SUMO-tagged protein was eluted with a 10 CV gradient of His-A buffer and His-C elution buffer (50 mM HEPES-NaOH pH 8.5, 500 mM NaCl, 500 mM Imidazole). For tag cleavage, the eluate was supplemented with 100 µg of PreScission™ protease and dialyzed against dialysis buffer-A (50 mM HEPES-NaOH pH 7.5, 500 mM NaCl, 1 mM DTT) over night. Cleaved protein was run on a subtractive HisTrap FF column and the protein-containing flow through was collected and concentrated. Protein was loaded onto a size exclusion chromatography column (Superdex 75, 10/300 gl) equilibrated in SEC-A buffer (50 mM HEPES-NaOH pH 7.5, 500 mM NaCl). Protein concentrations were determined by measurement of the A_{280}. Aliquots were flash frozen in liquid nitrogen and stored at -80 °C.

For central and fusion domain, lysis buffer-B was used (500 mM NaCl, 50 mM HEPES-NaOH pH 7.5, 0.1 % (v/v) Tween, 20 mM Imidazol, 10 % Glycerol). Moreover, all buffers contained HEPES-NaOH with pH 7.5 and for the final size exclusion chromatography a Superdex 200 column (16/600) and SEC-B buffer were used (50 mM HEPES-NaOH pH 7.5, 500 mM NaCl, 1 mM DTT). Fusion domain was otherwise purified like hTRMT2A RBD. The SUMO-tag of the central domain was not cleaved due to subsequent protein degradation. Instead, after over night dialysis in dialysis buffer-B (50 mM HEPES-NaOH pH 7.5, 150 mM NaCl, 1 mM DTT) the protein was loaded onto a HiTrap Heparin column equilibrated with dialysis buffer-B and eluted with Hep-B elution buffer (50 mM HEPES-NaOH pH 7.5, 1000 mM NaCl, 1 mM DTT). Protein containing fractions were proceeded as described above. Pooled protein peak fractions were concentrated to 2-5 mg/mL with a centrifugal filter (Amicon), flash-frozen in liquid nitrogen and aliquots were stored at -80 °C.

Primers for cloning and mutagenesis are listed in **Supplementary Table 1**

Human TRMT2A FL cloning, expression in insect cells and purification. The Bac-to-Bac baculovirus expression system (Invitrogen) was employed for hTRMT2A FL expression. N-terminal SUMO-tag fused hTRMT2A FL and its mutants were cloned into the pFastBac vector. For transfection using the FuGene HD transfection reagent 1.5 µg bacmid DNA and 3 µL transfection reagent were

preincubated for 30 min in 200 µL Sf-900 medium at RT, then added dropwise to the Sf21 cells pre-seeded on 6-well plates with a density of $0.4*10^6$ cells/mL. Then cells were incubated for 4 days at 27.5 °C.

Supernatant of transfected cells from two 6-wells was used to infect 10 mL of Sf21 shaking cell culture at a density of $1.4*10^6$ cells/mL. After 3-4 days incubation at 27.5 °C, insect cells were harvested by centrifugation for 10 min at 4 °C with 2000 rpm (Hettich centrifuge Rotina 420R). Virus-containing supernatant P1 was steril-filtered using a 0.22 µm filter (Merck). To amplify the virus 1.5 mL P1 was added to 250 mL of Sf21 shaking cell culture at a density of $0.4*10^6$ cells/mL. After another 3-4 days incubation at 27.5 °C, cells were harvested. The virus-containing supernatant P2 was sterile filtered and stored at 4 °C. Protein was expressed in Hi5 insect cells by adding 20 mL of P2 to 500 mL shaking culture at a density of $1*10^6$ cells/mL. Proteins were expressed in Hi5 insect cells for 2-3 days at 27.5 °C.

Cells were harvested by centrifugation (2000 x *g*, 15 min, 4 °C) and resuspended in lysis buffer-C (500 mM NaCl, 50 mM HEPES-NaOH pH 7.5, 0.1 % (v/v) Tween, 10 % Glycerol, 20 mM Imidazol). Next, insect cells were lysed using a dounce homogenizer. The lysate was clarified by centrifugation (40,000 x *g*, 30 min, 4 °C). Subsequent purification was performed as for hTRMT2A fusion domain with an initial HisTrap FF column, cleavage of the SUMO tag was followed by a subtractive HisTrap FF column, dialysis overnight with dialysis buffer-A and a final size exclusion chromatography run with a Superdex 200 column (16/600) in SEC-B buffer. hTRMT2A FL for crosslinking and mass spectrometry experiments was purified with SEC-C buffer (50 mM HEPES-NaOH pH 7.5, 500 mM NaCl, 0.5 mM TCEP), where DTT was exchanged by TCEP. Pooled protein peak fractions were concentrated to 2-5 mg/mL with a centrifugal filter (Amicon), flash-frozen in liquid nitrogen and aliquots were stored at -80 °C.

RNA in vitro transcription and purification. All RNAs were transcribed from a HPLC-purified forward primer, which contained the T7 RNA polymerase promoter region and a PAGE-purified reverse primer that consisted of the reverse complement DNA template and the T7 RNA polymerase promoter region (**Supplementary Table 2**). Briefly, 4 µM forward primer and 3.3 µM reverse primer were annealed in the presence of 20 mM MgCl2 for 5 min at 60 °C in a total volume of 1.2 mL and subsequently cooled to room temperature. 4 mM of each NTP, 16 mM MgCl2, 80 mg/mL PEG 800, 0.5 mg/mL T7 RNA Polymerase and 10X TRX-buffer (40 mM Tris/Cl pH 8.1, 1 mM spermidine, 0.01 % Triton X-100, 5 mM DTT) were added to the annealed primer-pair in a final volume of 5 mL. After incubation for 3 h at 37 °C, precipitate was removed by centrifugation for 10 min at 4 °C with 14,000 x g. Thereafter the RNA was precipitated with 0.1 volumes 3 M sodium acetate and 3.5 volumes ethanol for > 30 min at -20 °C. RNA pellets were resuspended in 0.5 mL DEPC-H2O and then 0.5 mL denaturing loading dye was added (2 mM Tris/Cl pH 7.5, 20 mM EDTA, 8 M urea, 0.025 % (w/v) bromophenol blue, 0.025 % (w/v) xylene cyanole). Separation on 8 % denaturing TBE-PAGE was followed by visualization of transcripts by UV shadowing and excision from gel. RNA was extracted by electroelution (Whatman Elutrap, GE Healthcare) at 200 V in 1X TBE according to manufacturer's instructions. Fractions containing the RNA were pooled dialyzed twice against 5 M NaCl and once against DEPC-H2O. RNAs were lyophilized, subsequently resuspended in DEPC-H2O and stored at -20 °C. General recommendations for working with RNAs were followed (Edelmann et al., 2014).

RNA radiolabelling and electromobility shift assays (EMSAs). *In vitro* transcribed RNA was 5' dephosphorylated using FastAP™ thermosensitive alkaline phosphatase (Thermo Scientific) according to manufacturer's recommendations. Thereafter, RNA was purified with Phenol-chloroform-isoamylalcohol extraction followed by isopropanol precipitation. 13 pmol of purified RNA was phosphorylated with y-^{32}P ATP (Hartmann Analytics) by T4 polynucleotide kinase (NEB) for 30 min at 37 °C. The enzyme was deactivated at 75 °C for 10 min and labeled RNA was purified with a NucAway Spin column (Ambion). To ensure proper RNA folding after each thawing cycle, RNA was denatured at 98 °C for 2 min and snap-cooled on ice prior to usage.

For 20 µL EMSA reactions increasing protein concentrations (0-25 µM) were incubated with 100 nM y-^{32}P labeled RNA in the presence of 2.5 ng/µL polyU competitor (poly-uridine ssRNA, Sigma) for 20 min at room temperature in RNAse-free EMSA-buffer (50 mM HEPES-NaOH pH 7.5, 150 mM NaCl, 4 % (v/v) glycerol). This results in a final concentration of 5 nM labelled RNA and 0-1.25 µM protein per reaction. Complexes were separated on 4 % native TBE-PAGE in TBE running buffer at 80 V. After gel fixation with 30 % (v/v) methanol and 10 % (v/v) acetic acid solution for 10 min, gels were dried in a vacuum gel dryer (model 573, BioRad). For analysis phosphor imaging plates were exposed to the radioactive dried gels for > 20 min and scanned with a FLA-300 system (Fujifilm). EMSAs were performed in triplicates on different days.

Methyltransferase Assay. hTRMT2A FL methylation activity was analyzed with the MTase-Glo™ assay (Promega). The assay was performed according to the manufacturer's instructions and experiments described in (Hsiao et al., 2016) in white-opaque OptiPlate™-384 (PerkinElmer). Experiments to determine K_m values were performed with increasing substrate concentrations. A final concentration of 5 µM hTRMT2A FL was incubated with final concentration of 0-6 µM *in vitro* transcribed tRNA and 20 µM SAM in 1X reaction buffer (20 mM Tris buffer pH 8.0, 50 mM NaCl, 1 mM EDTA, 3 mM $MgCl_2$, 0.1 mg/mL BSA, 1 mM DTT) for 60 min at room temperature. The reaction was stopped adding 0.5 % TFA (PanReac AppliChem). After 5 min incubation, 6X MTase-Glo reaction solution diluted in MilliQ-H_2O was added and incubated for 30 min at room temperature. Finally, MTase-Glo detection solution was added, incubated for 30 min in the dark at room temperature, and luminescence was read-out using a microplate reader (Perkin-Elmer). The data was transformed to display relative luminescence by subtracting the value of a negative control reaction without RNA. Data of triplicate measurements were plotted with R (version 4.1.0) and fitted with Michaelis Menten equation to obtain K_m values.

Crosslinking and Mass-spectrometry. For the first set of experiment complex reconstitution was performed; to do so *in vitro* transcribed $tRNA^{Gln}$ and recombinantly purified hTMRT2A FL were reconstituted in reconstitution buffer (50 mM HEPES-NaOH pH 7.5, 50 mM NaCl, 0.5 mM TCEP) in a 1:4 ratio. For the second set of experiments the complex was co-purified using size exclusion chromatography. Briefly, $tRNA^{Gln}$ and hTRMT2A FL were incubated in a 1:1 ratio on ice for 30 min. Then, the complex was separated from single RNA and protein using a S6 (15/150) column. For UV crosslinking, the *in vitro* reconstituted and co-purified complex was irradiated at 254 nm for 10 min on ice using an in-house built crosslinking apparatus as described previously (Kramer et al., 2014). For chemical crosslinking, mechlorethamine (NM, B1785, APExBIO Technology LLC) was added to a final

concentration of 1 mM following incubation for 30 min at 37 °C. Crosslinked samples were precipitated using ethanol and further processed as described in Kramer et al., 2014. In brief, 10 µg RNase A (EN0531, Thermo Fisher Scientific), 1 kU RNase T1 (EN0531, Thermo Fisher Scientific) and 250 U PierceTM universal nuclease (88700, Thermo Fisher Scientific) were used for tRNA digestion that was carried out for 2 h at 37 °C. Subsequently, proteins were digested using trypsin (V5111, Promega) at a 1:20 (enzyme to protein) mass ratio. After protein digestion, another 10 µg of RNase A and 1 kU of RNase T1 were added and the samples were incubated for 1 h at 37 °C. Free nucleotides and salts were removed using C18 columns (744601, Harvard Apparatus) and crosslinked peptides were enriched using in-house packed TiO_2 columns (Titansphere 5 µm; GL Sciences). Enriched peptides were dried and dissolved in 2 % (v/v) acetonitrile, 0.05 % (v/v) TFA. LS-MS/MS analyses were performed on a Thermo Scientific Orbitrap Exploris 480 mass spectrometer coupled to a nanoflow liquid chromatography system (Thermo Scientific Dionex Ultimate 3000). Peptide separation was performed over 58 min with a flow rate of 300 nl/min using a linear gradient and a buffer system consisting of 0.1 % (v/v) formic acid (buffer A) and 80 % (v/v) acetonitrile, 0.08 % (v/v) formic acid (buffer B). Peptide-nucleotide heteroconjugates were analysed in positive mode using a data-dependent top 30-acquisition method. MS1 and MS2 resolution were set to 120.000 and 30.000 FWHM, respectively. AGC targets were set to 10^6 (MS1) and 10^5 (MS2), normalized collision energy to 28, dynamic exclusion to 10 s, and maximal injection times to 60 ms (MS1) and 120 ms (MS2). Mass spectrometry data were analysed and manually validated using the OpenMS pipeline RNPxl and Open MS TOPPASViewer (Kramer et al., 2014). All crosslinks are listed in **Supplementary Table 3**.

Surface Plasmon Resonance (SPR). SPR studies were performed using a BIACORE 200 system (GE Healthcare). $tRNA^{Gln}$ was 3' biotin labeled with the Pierce ™ RNA 3' end biotin labeling kit (Thermo Fisher) according to manufacturer's recommendations. SA-chip (GE-Healthcare) was activated with three successive injections of 50 mM NaOH, before biotin labeled RNA diluted in DEPC-H_2O was coupled according to manufacturer's instruction. Analysis of RNA-protein interactions was performed at a flow rate of 10 µL/min in running buffer (150 mM NaCl, 50 mM HEPES-NaOH 7.5, 0.05 % (v/v) Tween). Analyte of interest was diluted in running buffer, injected for 3.5 minutes, and dissociated for 6 minutes. To remove any residual attached protein, 2x 2 minutes regeneration injections with 500 mM NaCl were done in between runs. Concentration series reached from 12.5 nM to 400 nM for hTRMT2A WT and 15.6 – 1000 nM for hTRMT2A IR protein. Data were analysed with the BIAevaluation software (GE Healthcare). Obtained binding curves were double-referenced against the signal in the empty reference channel and a buffer run. At equilibrium of the binding curves the corresponding response was plotted against analyte concentration. The K_D was determined by fitting this curve to a steady-state affinity model. All experiments were performed in triplicates.

Proximity-dependent biotinylation. BioID experiments were conducted to identify the hTRMT2A proximity interactome in HEK cells as described (Roux et al., 2013) with 5 replicates per condition. At 70 % cell confluency protein expression of BirA*-tagged protein of interest or BirA* tag alone was induced by addition of doxycycline. 6 h later 1 mL steril-filtered 20x DMEM/biotin was added to the cells to reach a final concentration of 50 µM biotin. Cells were incubated for 16-18 h. Prior to trypsination,

cells were washed three times with PBS. Detached cells ($8x10^7$ to $1x10^8$ per replicate) were centrifuged for 5 min at 4 °C with 300 x *g*. Cells were resuspended in 5 mL lysis buffer (50 mM Tris-HCl pH 7.4, 500 mM NaCl, 0.2 % SDS) freshly supplemented with 1:1000 benzonase (Thermo), 1 mM DTT and Pierce® Protease Inhibitor (Roche). Thereafter, cell suspension was incubated on a rotating wheel at 4 °C for 30 min. After 500 µL of 20 % Triton X-100 was added, the samples were sonicated for 1 min with 30 % duty cycle (Bandelin Sonopuls GM 70UV 70). Three sonication rounds were performed, and the samples incubated on ice for 5 min in between them. Before the third sonication round, 4.5 mL pre-chilled 50 mM Tris-HCl pH 7.4 was added. Sonicated samples were centrifuged for 10 min at 4 °C with 16,100 x *g*. 500 µL Dynabeads MyOne Streptavidin T7 magnetic beads (Thermo) per condition were equilibrated in 1.5 mL lysis buffer and 1.5 mL 50 mM Tris-HCl, pH 7.4. Beads were placed in a magnetic stand (DYNAL®, Invitrogen). Then, supernatant was removed by pipetting and the protein-containing supernatant from the centrifugation step was added to the equilibrated beads. Solution and beads were incubated on a turning wheel overnight at 4 °C. The supernatant was removed from the beads and substituted with 8 mL of wash buffer 1 (2 % SDS in MilliQ-H_2O). The wash step with wash buffer 1 was repeated. Next, beads were washed once with wash buffer 2 (0.1 sodium deoxycholate, 1 % Triton X-100, 1 mM EDTA, 500 mM NaCl, 50 mM HEPES-NaOH pH 7.5) and wash buffer 3 (0.5 % sodium deoxycholate, 0.5 % NP-40, 1 mM EDTA, 250 mM LiCl, 10 mM Tris-HCl pH 7.4). To remove detergent, beads were washed three times with wash buffer 4 (1 mM EDTA, 20 mM NaCl, 50 mM Tris-HCl pH 7.4). Washed beads were resuspended in 1.5 mL of 50 mM Tris-HCl pH 7.4 and then put in magnetic stand to remove supernatant. For elution 50 µL 1x sample buffer (50 mM Tris-HCl pH 6.8, 12 % sucrose, 1 % SDS, 0.004 % bromophenol blue, 20 mM DTT) supplemented with 3 mM biotin was added to beads, mixed and incubated at 98 °C for 7 min. Subsequently, samples were placed in magnetic stand and supernatant subjected to mass spectrometry or analytical Western blot analysis. Enriched and depleted proteins are listed in **Supplementary Table 4**.

Co-Immunoprecipitation. Co-IP experiments were performed to identify the hTRMT2A proteome in HEK cells with 5 replicates per condition. At 70 % cell confluence protein expression of protein of interest or FLAG tag alone was induced with doxycycline. 16-18 h later GFP expression was inspected with fluorescence microscopy and cells were washed twice with PBS. For cell harvest, 10 mL ice-cold PBS was added and cells scraped off the plate. Cell suspension was centrifuged for 5 min at 4 °C with 300 x *g*. Pellets were flash-frozen in liquid nitrogen to ensure equal sample time point.

Cell pellets were thawed and resuspended in 1 mL lysis buffer (50 mM Tris-HCl pH 7.8, 150 mM NaCl, 1 mM EDTA, 1 % Triton X-100) supplemented with one tablet Pierce® Protease Inhibitor (per 100 mL lysis buffer). Suspension was transferred to a new tube and centrifuged for 10 min at 4 °C with 16,100 x *g*. Meanwhile, 50 µL Anti-FLAG® M2 Magnetic Beads (Merck) were equilibrated two times with 900 µL TBS (50 mM Tris-HCl pH 7.8, 150 mM Nacl) and three times with 900 µL lysis buffer. In between wash steps the beads were incubated for 3 min on a magnetic stand (DynaMag 2, DYNAL®, Invitrogen). Then, 3.5 mg protein from the supernatant of the centrifugation step were added to the equlibrated beads. Protein concentration was measured with the Bradford assay solution (Roth) according to instructions. Beads were incubated for 1 h at 4 °C in the shaking mode on a rotator wheel. Therafter, unbound protein was removed by washing three times with 900 µL high salt wash buffer (50 mM Tris-

HCl pH 7.8, 250 mM NaCl, 1 mM EDTA, 1x Triton X-100). The third wash step was incubated for 5 min at 4 °C in shaking mode on a rotator wheel. To remove detergent, beads were washed three times with 900 µL 50 mM Tris-HCl, pH 7.8. Beads were distributed to two tubes for elution: 900 µL for mass spectrometry and 100 µL for Western blot analysis. Elution was performed by addition of 20 µL 2x Laemmli buffer (4 % (w/v) SDS, 20 % glucose, 0.004 % bromophenol blue, 125 mM Tris-HCl pH 6.8) and incubation for 10 min at 98 °C. Finally, tubes were placed into the magnetic stand and the supernatant transferred to a new tube for respective mass spectrometry analysis and analytical Western blot analysis. Enriched and depleted proteins are listed in **Supplementary Table 5**.

Western blot analysis

Western blot of BioID and Co-IP samples. From BioID and Co-IP experiments, sample was mixed with SDS loading buffer (110 mM Tris-HCl pH 6.8, 40 % (v/v) glycerine, 40 mM DTT, 4 % (w/v) SDS, 0.25 % (w/v) bromophenol blue) and heated for 10 min to 95 °C. Next, samples were loaded on a NuPAGE 4-12 % Bis-Tris gradient gels (Invitrogen) and run with 1x NuPAGE MOPS SDS running buffer (Invitrogen) for 1 h at 180 V. Prior to run 500 µL NuPAGE antioxidant (Invitrogen) was added. Proteins were transferred to a PVDF membrane (Thermo) in an Invitrogen Western blot blot chamber. PVDF membrane was pre-activated for 1 min in MeOH. All blotting components were soaked with 1x NuPAGE transfer buffer before assembly. Western blot was run for 1.5 h at 30 V. Successful blotting was probed with Ponceau S staining. Thereafter, blots were rinsed with MilliQ-H_2O and blocked for 30 min using 1 % Casein in PBS-T (1 % Tween in PBS). After blocking, the solution was substituted by primary antibody diluted in 0.5 % Casein in PBS-T and incubated ON at 4 °C (anti-H3 – abcam ab1791, polyclonal rat, 1:10.000; anit-Flag – in-house antibody, IgG1, monoclonal rat, 1:10). Next, blot was washed three times for 5 min in PBS-T. In case of anti-Streptavidin-HRP antibody (Thermo, N100, 1:10.000) the blot was washed five times for 5 min and thereafter directly visualized. The secondary antibodies were diluted in PBS-T and incubated for 1 h at RT (goat-anti-rabbit-HRP – abcam6721, polyclonal goat, 1:10.000; mouse-anti-rat-HRP, in-house antibody, polyclonal mouse, 1:1000). Three 5 min washing steps with PBS-T were performed before visualization of blots. The Pierce®ECL Western blotting kit (Thermo) was used for visualization according to manufacturer's recommendations using the Fusion SL 4 device and software (Vilber Lourmat).

Western blot of BioID cell lines and TRMT2A KD cell lines. 20-50 µg of the cell lysates were supplemented with Laemmli buffer and boiled (95 °C for 5 min). Samples were subjected to SDS-PAGE (100 V for 90 min) and transferred onto nitrocellulose membrane (225 mA per gel for 60 min) by semi-dry blotting. The membranes were blocked (5% skimmed milk in TBS-T for 60 min) and incubated with the primary antibody at 4°C overnight. Membranes were washed three times for 10 min in TBS-T and incubated with the secondary horse radish peroxidase (HRP) coupled antibody for two hours at room temperature. Subsequently, the membranes were washed three times in TBS-T for 10 min, and the chemiluminescence signal was detected using the Super Signal® West Femto Maximum Sensitivity Substrate (Thermo Scientific) detection kit according to manufacturer's instructions. Chemiluminescence signals were visualized using the Alliance UVltec system (Biometra). Primary antibodies used: rabbit anti-TRMT2A (1:1000; Sigma #HPA001077); mouse anti-Actin (1:1000; Abcam #ab3280); mouse anti-FLAG (1:2000; Sigma #F3165). Secondary HRP-coupled antibodies were: sheep

anti-mouse (1:10,000; GE Healthcare #NXA931V) or donkey anti-rabbit (1:10,000; GE Healthcare #NA934V), respectively.

LS-MS/MS analysis of BioID and Co-IP samples. Proteins were proteolysed with LysC and trypsin with filter-aided sample preparation procedure (FASP) as described (Wiśniewski et al., 2009; Grosche et al., 2016). Acidified eluted peptides were analyzed on a QExactive HF-X mass spectrometer (Thermo Fisher Scientific) online coupled to a UItimate 3000 RSLC nano-HPLC (Dionex). Samples were automatically injected and loaded onto the C18 trap cartridge and after 5 min eluted and separated on the C18 analytical column (Acquity UPLC M-Class HSS T3 Column, 1.8 µm, 75 µm x 250 mm; Waters) by a 95 min non-linear acetonitrile gradient at a flow rate of 250 nl/min. MS spectra were recorded at a resolution of 60000 with an automatic gain control (AGC) target of 3e6 and a maximum injection time of 30 ms from 300 to 1500 m/z. From the MS scan, the 15 most abundant peptide ions were selected for fragmentation via HCD with a normalized collision energy of 28, an isolation window of 1.6 m/z, and a dynamic exclusion of 30 s. MS/MS spectra were recorded at a resolution of 15000 with a AGC target of 1e5 and a maximum injection time of 50 ms. Unassigned charges, and charges of +1 and >8 were excluded from precursor selection.
Data processing protocol. Raw spectra were imported into Progenesis QI software (version 4.1). After feature alignment and normalization, spectra were exported as Mascot Generic files and searched against the human UniProt database (20,434 sequences) with Mascot (Matrix Science, version 2.6.2) with the following search parameters: 10 ppm peptide mass tolerance and 20 mmu fragment mass tolerance, one missed cleavage allowed, carbamidomethylation was set as fixed modification, methionine oxidation, and asparagine or glutamine deamidation were allowed as variable modifications. A Mascot-integrated decoy database search calculated an average false discovery of <1% when searches were performed with a mascot percolator score cut-off of 13 and an appropriate significance threshold p. Peptide assignments were re-imported into the Progenesis QI software and the abundances of all unique peptides allocated to each protein were summed up. The resulting normalized abundances of the individual proteins were used for calculation of fold-changes of protein ratios between conditions. Proteins with a sample/control ratio of at least 4 were considered differentially abundant. Statistical analysis was performed on log2 transformed normalized abundance values using Student's t-test. Changes in protein expression between conditions were considered significant at $p < 0.05$. Principal component analysis was performed in Progenesis QI software.

GO-term analysis. „Biological processes“ (BP) and „cellular compartements“ (CC) gene ontology (GO) term analysis was performed with data from BioID experiments using the GO enrichment analysis tool from gene ontology using the PANTHER databank (Mi et al., 2013). UniProt protein names of significantly enriched hits from BioID experiments were used for GO enrichment analysis. Significance of GO-term enrichment was calculated as false discovery rate (FDR) with the Fisher’s exact test. Using custom R-scripts a bubble diagram was generated that visualizes enrichment for respective GO-term on x-axis, the significance of enrichment with color code and the counts per GO-term with node size.

Generation of BioID and Co-IP stably transfected cell lines. For stable transfection of HEK cells a piggyBac (PB) transposon plasmid was used (Li et al., 2013; Krendl et al., 2017). Co-transfection with the PB helper plasmid, encoding for PB transposase, allows for stable insertion of the gene of interest into the chromosome. Protein expression can be induced by doxycyline administration (Li et al., 2013; Krendl et al., 2017). For transfection HEK cells were plated in a 6-well plate and grown to 80 % confluency. According to the Lipofectamine™ 3000 transfection kit manual (Invitrogen), two solutions were prepared. Solution 1 contained Lipofectamine 3000 in OptiMEM medium (Gibco). Solution 2 contained P3000™ reagent, 2.5 µg of PB plasmid with the gene of interest, 2.5 µg helper plasmid in OptiMEM. Both solutions were mixed and incubated for 15 min at room temperature. HEK cells were washed two times with PBS and fresh complete medium (90 % DMEM (v/v), 10 % FBS (v/v), 1 % Pen/Strep) was added. After the incubation period of the lipofection solution, it was dropwise added to the cells and incubated for 3 days. For antibiotic selection complete medium supplemented with hygromycin B (0.7 mg/mL, Invitrogen) was added and exchanged 2-3 times a week for stable integration of the PB plasmid into the genome.

The same expression level of the protein of interest was achieved by fluorescence-activated cell sorting (FACS). Protein expression in cells was induced with doxycycline 18 h before FACS experiment. For FACS the cells were detached with trpysin, washed twice with PBS for 5 min and resuspended in sterile FACS buffer (0.5 % BSA, 2 mM EDTA, 25 mM HEPES-NaOH pH 7.5 in PBS). Directly prior to FACS experiment the cells were passed through a 35 µm cell strainer. First gating step subtracted dead cells and aggregates. A second gate was set to sort the cell population with a low GFP signal. Sorted cells were plated in 6-well plates and propagated with complete medium containing hygromycin-B.

Generation of stable RNAi-mediated KD of hTRMT2A. Stable RNAi-mediated knockdown of hTRMT2A was achieved as described earlier (Margreiter et al., 2022). HEK293t cells were infected with commercially available Lentiviral particles for hTRMT2A KD and scrambled control cell line (MISSION® shRNA Lentviral Transduction Particles: scrambled control WT = SHC002V, KD1 = NM_182984.2-**856**s1c1, KD2 = NM_182984.2-**1574**s1c1; Sigma-Aldrich). Cells with stable integration of shRNA were selected as puromycin-resistant colonies. hTRMT2A silencing effect was probed by Western blotting.

Ribosome isolation and mass spectrometry analysis of rRNA modification status. Ribosome isolation from HEK cells was performed according to a protocol published earlier (Belin et al., 2010). Briefly, 80 % confluent HEK cells were harvested in ice cold PBS and centrifugated at 4 °C. Cell pellet was resuspended in equivolume buffer A (250 mM sucrose, 250 mM KCl, 5 mM $MgCl_2$, 50 mM Tris-HCl pH 7.4). This step was repeated twice. For cell lysis 0.7 % (v/v) NP-40 was added and incubated on ice for 10-15 min. To separate nuclei, cell lysate was centrifugated for 10 min at 750 x *g* and 4 °C. To prepare fraction without mitochondria, the supernatant was centrifugated for 10 min at 12,500 x *g* and 4 °C. Post-mitochondrial fraction (PTM) supernatant was transferred to a new tube. According to PTM volume the KCl concentration was carefully adjusted to 500 mM using a 4 M stock solution. Adjusted PTM was carefully layered on top of a 2 mL sucrose cushion (1 M sucrose, 500 mM KCl, 4 mM $MgCl_2$, 50 mM Tris-HCl pH 7.5). For balancing polycarbonate tubes prior to ultracentrifugation buffer B was used (250 mM sucrose, 500 mM KCl, 5 mM $MgCl_2$, 50 mM Tris-HCl pH 7.4). Samples were

ultracentrifugated for 2 h at 250,000 x *g* and 4 °C. Supernatant was discarded and translucent ribosome pellet was washed 200 µL with cold DEPC-treated H2O. Finally, ribosomes were resuspended in 3x 100 µL buffer C (25 mM KCl, 5 mM $MgCl_2$, 50 mM Tris-HCl pH 7.4).

For rRNA isolation, 100 µL of ribosomes diluted in buffer C, were mixed with 15 µL DEPC-H_2O and 15 µL 3 M NaOAc. Next, 1 volume phenol-chloroform-isoamylacohol (25:24:1) was added. After centrifugation for 1 min at 16,100 x *g*, upper aqueous phase was transferred to new tube and mixed with 1 volume chloroform. The recovered upper phase from this purification step was precipitated in presence of 0.5 µL RNA-grade glycogen and 2 volumes ethanol for > 20 min at -20 °C. RNA was pelleted for > 20 min at 16,100 x *g* and 4 °C. Dry pellet was resuspended in 20 µL DEPC-H_2O. Integrity and purity of rRNA was checked with denaturing PAGE and Agilent Tape station measurements.

rRNA digestion to the nucleoside level

Samples containing 10 µg of rRNA were enzymatically digested to the nucleoside level using the Nucleoside Digestion Mix of New England Biolabs: Therefore, a ~110 ng/µL solution of the rRNA in nuclease-free water was prepared. 90.0 µL per sample was mixed with 12 µL of Nucleoside Digestion Mix Reaction Buffer (10x, New England BioLabs), an aqueous solution of the isotope standard $^{13}C_5$-m^5U (5 pmoL; 13µL), and 5 µL of Nucleoside Digestion Mix (New England BioLabs). The mixture was incubated for 1.5 h at 37 °C. All samples were filtrated using an AcroPrep Advance 96 filter plate 0.2 µm Supor from Pall Life Sciences and subsequently analyzed by LC-MS. Samples were kept on ice during handling.

Liquid chromatography – mass spectrometry (LC-MS) of rRNA

The HPLC-HESI-MS analyses were performed on a Dionex Ultimate 3000 HPLC system coupled to a Thermo Fisher LTQ Orbitrap XL mass spectrometer. Compounds of interest (injection volume: 85 µL) were separated with an Interchim Uptisphere120-3HDO C18 column, the temperature was maintained at 30 °C. LC-MS buffers were aqueous buffer A (2 mM NH_4HCOO in H_2O; pH 5.5) and organic buffer B (2 mM NH_4HCOO in H_2O/MeCN 20/80 v/v; pH 5.5). The gradient was as follows: 0→10 min, 0 % B; 10→50 min, 0→5 % B; 50→52 min, 5→100 % B; 52→55 min, 100% B with a flow rate of 150 µL/min. The UV chromatogram was recorded at 260 nm with a Dionex Ultimate 3000 Diode Array Detector with a data collection rate of 20 Hz and a response time of 0.10 s. The chromatographic eluent was directly injected into the ion source of the mass spectrometer without prior splitting. Ions were scanned in the positive polarity mode over a full-scan range of m/z = 225-2000 with a resolution of 100,000. Parameters of the mass spectrometer were tuned with a freshly mixed solution of inosine (5 µM) in LC-MS buffer A. Source-dependent parameters were set as follows: Capillary temperature 275 °C; APCI vaporizer temperature 100 °C; sheath gas flow 5.00; auxiliary gas flow 21.0; sweep gas flow 1.00; source voltage 4.80 kV; capillary voltage 0 V; tube lens voltage 45.00 V. Data analysis was performed using the program Xcalibur from Thermo Scientific: Ion chromatograms of m^5U and $^{13}C_5$-m^5U were extracted from the total ion current (TIC) chromatogram with a mass range set to +/- 0.0050 u around the exact mass $[M+H]^+$ of the compound of interest, and the peak area ratio of m^5U versus $^{13}C_5$-m^5U was calculated. Furthermore, this ratio was normalized to the amount of adenosine in the sample which was calculated

from its peak area in the UV chromatogram using a calibration curve (The amount of adenosine in the sample was taken as a proxy for the exact amount of rRNA in the sample).

Immunostainings. Immunocytochemistry (ICC) experiments were performed to determine hTRMT2A localization in HEK cells. Cells on coverslips were fixed for 10 min at RT using 3.7 % fromaldehyde solution in PBS. After two PBS washing steps, cells were permeabilized for 5 min with 0.5 % Triton X-100 in PBS. Next, cells were blocked for 30 min using blocking buffer (1 % goat serum in PBS-T). Primary antibody (BirA Antibody, Novus Biologicals 5B11c3-3 or FLAG Antibody 6F7, HMGU) diluted in PBS was added for 1 h at RT. After three washing steps with PBS-T, cells were incubated with secondary (Goat anti-Mouse IgG Alexa Fluor 647, Invitrogen A-21235 or Goat anti-Rat IgG Alexa Fluor 647, Invitrogen A-21247) antibody diluted in blocking buffer for 1 h at RT in the dark. Cells were washed three times with PBS-T. Thereafter, cell nucleus was stained with DAPI at a concentration of 0.5 µg/mL DAPI (Thermo) in PBS for 5 min at RT and washed two times with PBS. Finally, coverslips were mounted using the ProLong™ Diamond Antifade Mountant (Invitrogen). Cells were imaged with the Leica DMi8 fluorescence microsocope and the Leica imaging software. Images were analyzed with the Fiji ImageJ software.

Dual luciferase translation assay. The dual Luciferase assay to probe translational fidelity was performed using three Renilla-Firefly fusion protein constructs. In two Renilla sequences mutations were introduced at residues crucial for luciferase activity (Javid et al., 2014).
hTRMT2A WT (scrambled control) as well as KD1 and KD2 (scrambled control) were cultured (Gibco™ DMEM + 10% Gibco™ FBS + 1% Gibco™ Antibiotic-Antimycotic) and seeded at a density of 20,000 cells per well in a 96-well-plate suitable for luminescence measurements (greiner bio-one #655075). Cells were transfected with Renilla and Firefly fusion constructs (WT, D120N, E145Q) using *Trans*IT®-LT1 Transfection Reagent (Mirus Bio) according to the manufacturer´s instructions. After 48 h of incubation at 37 °C and 5 % CO_2 culture medium was exchanged with fresh growth medium and Luciferase activity was measured with the Dual-Glo® Luciferase Assay Kit (Promega) according to manufacturer´s instructions using the Tecan Spark® plate reader. Integration time was 10 s. Data represent mean ± SD of 6 biological replicates, in technical triplicates. Statistical analysis was performed with the Wilcoxon rank test and student's t-test in R (version 1.4.).

Results

TRMT2A shows low binding specificity for its physiological target tRNAs

To understand how specificity of tRNA methylation is achieved by hTRMT2A, it is imperative to assess both, RNA binding and catalytic activity of hTRMT2A (Carter et al., 2019). For *in vitro* characterization of the TRMT2A-binding preferences, we prepared recombinant human TRMT2A full-length (hTRMT2A FL) and different *in vitro* transcribed RNAs (**Supplementary Figure 1A**). We assessed binding with an Electrophoretic Mobility Shift Assay (EMSA), where ^{32}P-labelled RNA was preincubated with increasing concentrations of hTRMT2A FL and polyU as competitor to preclude non-specific binding. To explore how important the uridine in position 54 of a given tRNA is for binding, we included two tRNAs with U54 ($tRNA^{Gln}$, $tRNA^{Phe}$) and two tRNAs lacking U54. The latter consisted of $tRNA^{Ala}$ with A54 and a mutant version of $tRNA^{Gln}$ where U54 had been changed into G ($tRNA^{Gln\ U54G}$). hTRMT2A FL bound all these tRNA with apparent equilibrium dissociation constants (K_D) in a low nanomolar range (**Figure 1A**). A somewhat stronger binding was observed for $tRNA^{Gln}$, where a shifted band was already observed at a protein concentration of 60 nM. Of note, for all tRNAs except for $tRNA^{Phe}$ we observed supershifts that imply multiple hTRMT2A enzymes to bind to respective RNA. However, since these supershifts only occurred at higher, micro-molar protein concentrations, we assume that they represent unspecific oligomerization without physiological importance. Also, for the negative control polyU-RNA the binding appeared only as a smear and not as specific band shift, indicative of a rather unspecific interaction (**Figure 1B**).

In order to dissect the structural requirements for hTRMT2A FL binding, we also performed EMSAs with the $tRNA^{Gln}$ T-Loop and two structured fragments derived from mRNA: a fragment of the KCND2 mRNA, which consists of the previously published stem-loop target of hTRMT2A (Carter et al., 2019). Moreover, the unrelated E3 stem-loop of the *S. cerevisiae ASH1* mRNA, which is not known to be methylated by hTRMT2A, but contains the previously identified sequence motif in the predicted loop recognized by hTRMT2A (**Supplementary Figure 2**) (Edelmann et al., 2017; Carter et al., 2019). The $tRNA^{Gln}$ T-Loop showed a weaker shift with most of the RNA remaining in its free form, which suggests the formation of complexes with lower stability (**Figure 1B**). Both stem-loop containing mRNAs displayed binding, however in a high nanomolar to micromolar K_D range (**Figure 1B**), which indicates lower affinity than observed with tRNAs.

In summary, these results suggest that hTRMT2A FL binding to tRNAs is independent of the presence of a U54 as potential methylation site and that the enzyme binds stem-loop structured RNAs with modestly lower affinities than tRNAs. While binding affinities are in the expected range (Keffer-Wilkes et al., 2020), binding specificity of hTRMT2A for its physiological methylation targets appears to be low *in vitro*.

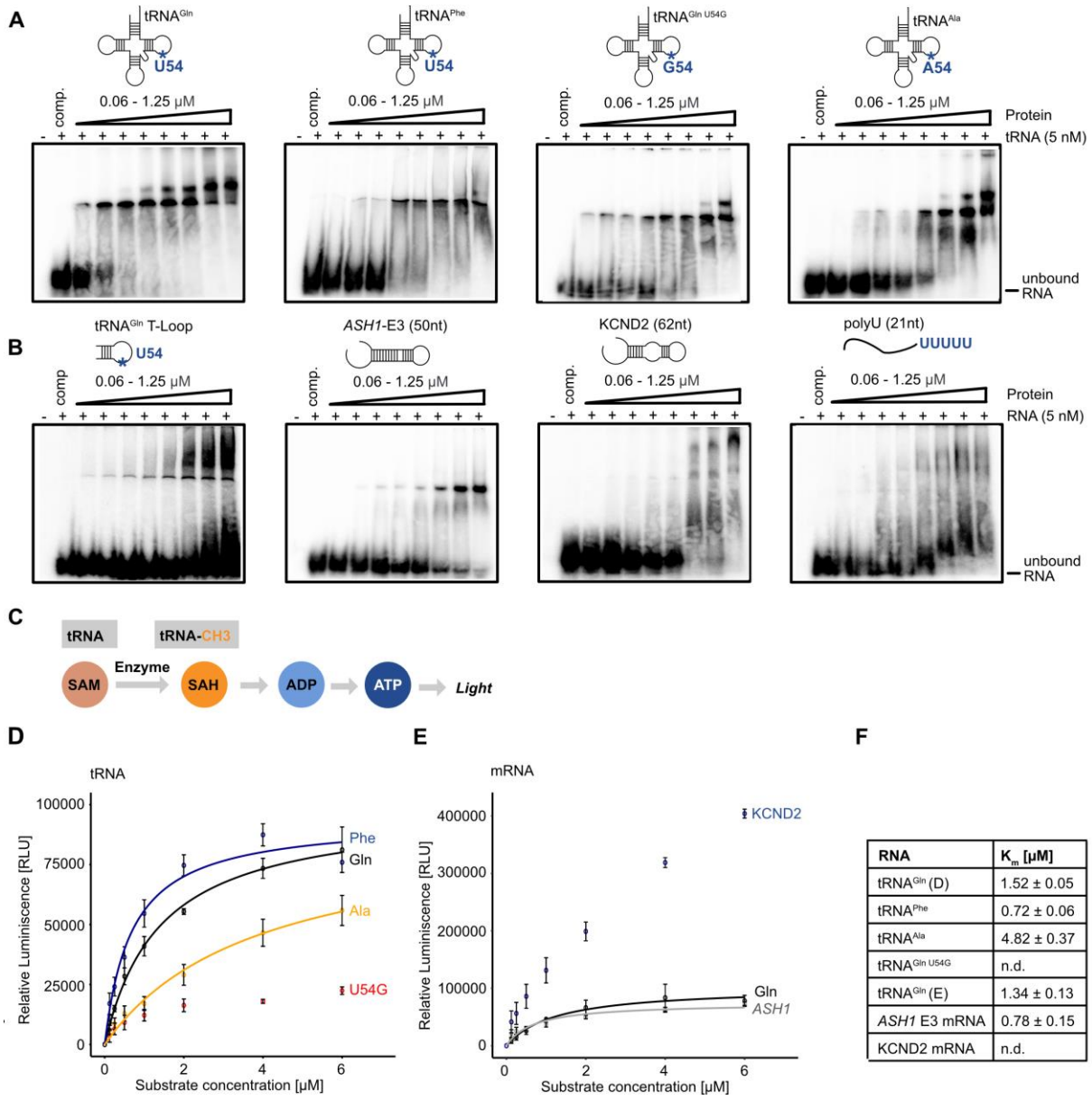

RNA	K_m [µM]
$tRNA^{Gln}$ (D)	1.52 ± 0.05
$tRNA^{Phe}$	0.72 ± 0.06
$tRNA^{Ala}$	4.82 ± 0.37
$tRNA^{Gln\ U54G}$	n.d.
$tRNA^{Gln}$ (E)	1.34 ± 0.13
ASH1 E3 mRNA	0.78 ± 0.15
KCND2 mRNA	n.d.

Figure 1 – hTRMT2A FL (aa 1-625) binds and methylates RNA with low specificity.
A EMSAs of tRNA with differing nucleotides at position 54 shows for all tRNA high affinity binding in low nanomolar K_D range. **B** EMSA of truncated $tRNA^{Gln}$ T-loop displays unspecific binding with unbound RNA at high protein concentrations. EMSA with mRNA derived from *S. cerevisiae ASH1* E3 element (1771-1821; 51nt) shows binding in nanomolar K_D range. EMSA with mRNA derived from human KCND2 (chr7: 366813-366875; 62nt) shows binding in micromolar K_D range, whereas control experiment using polyU (21 nt) shows no binding. Binding assays were performed with ^{32}P labelled RNA. For experiments polyU competitor and labelled RNA were pre-incubated with increasing concentrations of hTRMT2A FL for 20 min. Reaction without protein served as control. Free RNA and RNA-protein complex were separated on 4% native PAGE. Each experiment was performed in triplicates. **C** Principle of the MTase Glo™ Methyltransferase assay for methylation experiments. **D** Results of tRNA methylation experiments. **E** Results of mRNA methylation experiments. Data represent mean ± SD for three replicates. Curves were fitted with Michaelis-Menten equation illustrated as lines. **F** Listed K_m values from Michaelis-Menten fitting. For methylation experiments hTRMT2A FL and methyl-donor SAM were preincubated with increasing concentrations of *in vitro* transcribed RNAs for 1 h. Reaction without RNA served as control.

Enzymatic activity of hTRMT2A FL

To correlate our binding studies with enzymatic activities, we tested the methyltransferase activity of hTRMT2A FL on selected RNAs using the luminescence based MTase Glo™ assay (**Figure 1C**). In this assay, relative luminescence correlates directly with enzymatic activity. hTRMT2A FL was incubated with increasing RNA concentrations to generate saturated K_m curves for Michaelis-Menten fitting. A reaction without RNA was used as background control. We observed that hTRMT2A methylates $tRNA^{Gln}$ and $tRNA^{Phe}$ with a K_m of 1.52 ± 0.05 µM and 0.72 ± 0.06 µM, respectively, which is in the range of previously reported K_m values for methyltransferases (Swinehart et al., 2013). In contrast, the two tRNAs lacking U54 ($tRNA^{Ala}$, $tRNA^{Gln\ U54G}$) were methylated orders of magnitude less efficiently (**Figure 1D**). Taken together, binding assays and enzymatic assays indicate that specificity of target-RNA methylation is mainly mediated by a uridine residue in the right position and not by the affinity to these tRNAs per se. In agreement with our binding experiments (**Figure 1B**), KCND2 mRNA was required in high concentrations and did not reach saturation indicating non-physiologically relevant enzymatic activity of hTRMT2A on KCND2 mRNA. The presence of the hTRMT2A sequence recognition motif in the unrelated, stem-loop structured *ASH1* E3 mRNA was sufficient for similar methylation like those of tRNA substrates with a K_m of 0.78 ± 0.15 (**Figure 1D, Supplementary Figure 2**). Thus, hTRMT2A cannot only methylate substrate tRNA, but also other stem-loop structured RNAs.

tRNA is bound by hTRMT2A via multidomain interactions

Based on the results from binding and methylation experiments we choose $tRNA^{Gln}$ to dissect the RNA-interacting domains of hTRMT2A. For this purpose we generated several hTRMT2A fragments, whose domain borders were chosen based on experimental evidence (Margreiter et al., 2022), sequence alignments and homology models. We purified hTRMT2A FL, the RNA-binding domain (RBD, aa 69-147) and the central domain (Central, aa 237-414). Unfortunately, the predicted entire methyltransferase domain (aa 179-581) was unsuitable for *in vitro* studies due to protein degradation. Instead, we created a more stable protein fragment, in which the RBD is fused directly to a part of the methyltransferase domain (Fusion, 69-240/413-590) (**Figure 2A**, **Supplementary Figure 1C/D**). In EMSAs all fragments showed only weak mobility shifts in the micromolar protein range (**Figure 2C**) and hence much weaker binding than hTRMT2A FL (**Figure 2B**). This indicates that none of the individual domains - RBD, Central and Fusion – are sufficient for full $tRNA^{Gln}$ binding and that they might have to interact cooperatively for physiological binding affinity.

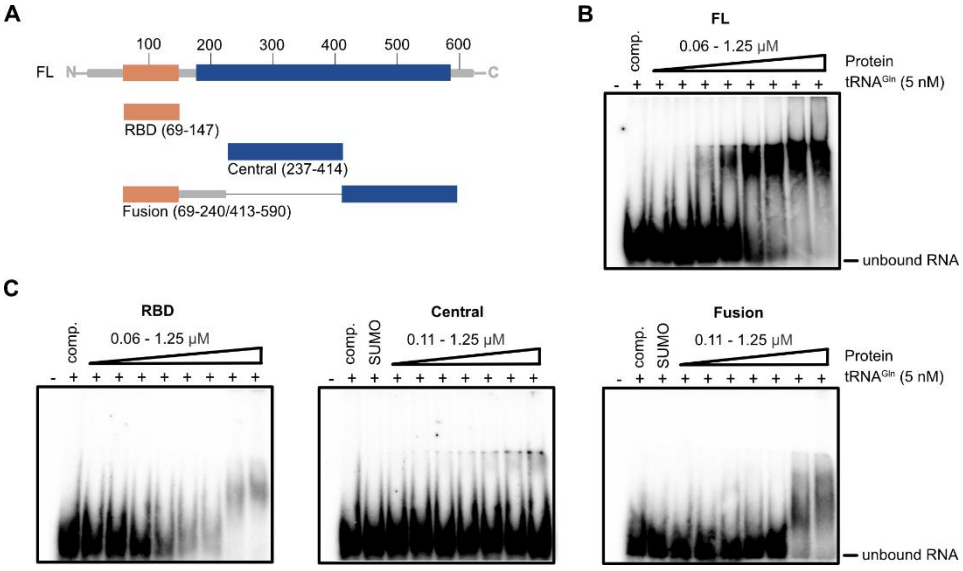

Figure 2 – hTRMT2A domains bind tRNA^{Gln} cooperatively.
A Cartoon depicting protein fragments of hTRMT2A used for EMSAs. **B** EMSA with hTRMT2A FL shows high affinity binding to tRNA^{Gln} in nanomolar K_D range. **C** EMSA with hTRMT2A RBD, Central and Fusion domain displays only low affinity binding to tRNA^{Gln} in micromolar K_D range. Because the SUMO-tagged Central domain was used, a SUMO-tag control was included. Binding assays were performed with ^{32}P labelled tRNA^{Gln}. For experiments polyU competitor and labelled RNA were pre-incubated with increasing concentrations of hTRMT2A variants for 20 min. Reaction without protein served as control. Free RNA and RNA-protein complex were separated on 4% native PAGE. Each experiment was performed in triplicates.

tRNA binding requires interactions with all hTRMT2A domains

To map the hTRMT2A-tRNA^{Gln} interaction surface with near-single amino acid resolution, we performed nitrogen mustard (NM) and ultraviolet radiation (UV) induced cross-linking of the hTRMT2A-tRNA^{Gln} complex followed by mass spectrometry. Experiments were conducted with the *in vitro* reconstituted protein-RNA complex (**Supplementary Figure 3A**), as well as with the co-purified complex (**Figure 3A**, **Supplementary Figure 3B**). To confirm that hTRMT2A FL forms a stable complex with tRNA^{Gln}, we also performed size exclusion chromatography with tRNA^{Gln} and hTRMT2A FL separately and with the hTRMT2A-tRNA^{Gln} complex (1:1 ratio). Stable complex formation was apparent as a shift of the elution peak to smaller elution volumes (from 17.41 mL to 15.46 mL), corresponding to a higher molecular weight (**Figure 3A**).

The *in vitro* reconstituted and co-purified samples were cross-linked, trypsin- and RNase-digested, and analyzed by mass spectrometry. Out of the four collected datasets (UV, NM, *in vitro* reconstituted, purified complex) we consistently found in at least three of them the following amino acids to be cross-linked to RNA: C270 to a C base, C463 to A or U, H386 to U/C or G. Both C111 and H83 cross-linked to all four nucleotides (**Figure 3B**). In some instances, these amino acids also crosslinked to incompletely digested dinucleotides such as UU. Mapping of both crosslinked amino acids C111 and H83 onto the previously published X-ray structure of the RBD from hTRMT2A FL (Margreiter et al., 2022) shows tRNA interaction

with the ß-sheet surface (C111) and with one of the flexible loops (H83) (**Figure 3C**). For RBDs, the ß-sheet surface has been identified as the major RNA binding platform, although also loop-mediated RBD-RNA interactions have been reported (Cléry et al., 2008; Cléry et al., 2013). An electrostatic surface potential illustrates that C111 and H83 are both part of a positive-charged surface pre-dispositioned to bind RNA (**Figure 3D**).

The crosslinked amino acids C270, H386 and C463 are distributed across the methyltransferase domain. A sequence alignment with *E. coli* TrmA (**Supplementary Figure 4**) revealed that C463 of hTRMT2A corresponds to A241 of *E. coli* TrmA. In the *E. coli* TrmA T-Loop co-structure (PDB ID: 3BT7) residue A241 is close to the catalytic center and in proximity (below 10 Angstrom) to the stem of the T-Loop. Proximal to the crosslinked residue C270 lies G263, which corresponds to R51 of *E. coli* TrmA, a residue shown to modestly contribute to tRNA binding (Keffer-Wilkes et al., 2020).

In two of four datasets 17 additional cross-linked residues were identified (**Supplementary Figure 3C**). Most notably, amongst them is the catalytic cysteine C538 cross-linked to uridine. Since C538 is known to make a covalent bond to the U54 base of the during catalysis (Carter et al., 2019), this highlights the specificity of our crosslinking mass spectrometry data. Taken together, these results cross-validate our previous observation from EMSAs that multiple domains are involved in and required for RNA binding.

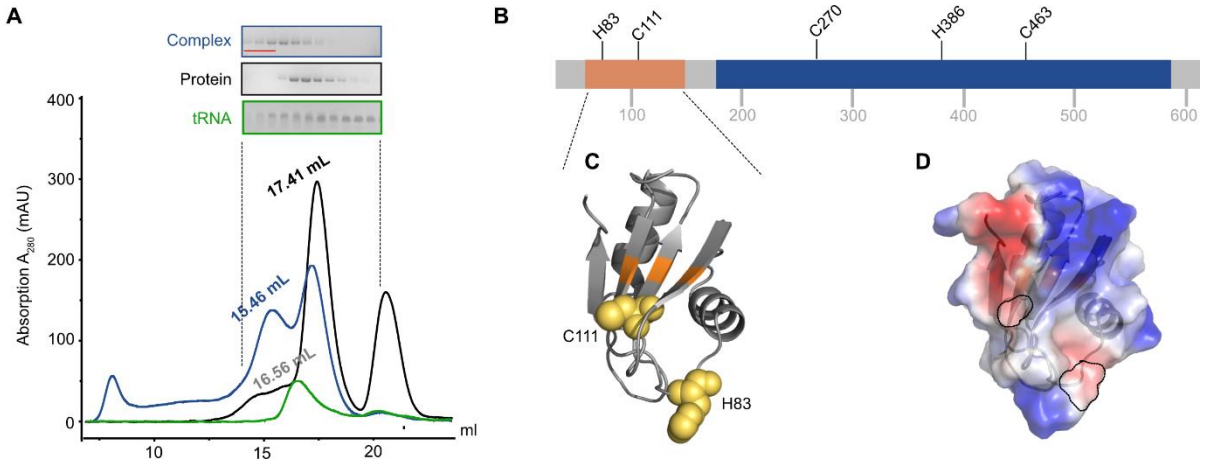

Figure 3 – tRNA^{Gln} contacts various amino acids from all hTRMT2A domains.
A Size exclusion chromatography profile from a size-exclusion chromatography run with an S6 (15/150) column with hTRMT2A FL and tRNA^{Gln}, as well as the stable protein-RNA 1:1 complex. SDS-PAGE and denaturing PAGE of protein, RNA and complex are shown. Pooled fractions for crosslinking experiments are highlighted in red. **B** Crosslinked amino acids are mapped on a linear representation of hTRMT2A FL and those consistently crosslinked in three or four of four datasets are shown. **C** Crosslinked amino acids (yellow) are mapped on the hTRMT2A RBD X-ray structure (PDB ID: 7NTO) and the predicted RNA binding surface is colored orange. **D** Electrostatic surface potential of hTRMT2A RBD shows crosslinked amino acids (dashed lines) being located on a positively charged patch. Figures were prepared with PyMOL (version 2.0.4).

An RNA-binding deficient mutant of hTRMT2A FL

To better dissect the function of hTRMT2A, we decided to create a mutant version of this enzyme with impaired RNA-binding activity. Based on the EMSAs with subdomains of hTRMT2A (**Figure 2**) and our cross-linking experiments (**Figure 3**), we anticipated that an RNA-binding deficient mutant of hTRMT2A would require surface mutations in the RBD and across the methyltransferase domain and choose these areas for mutation. For selecting the exact amino acids, sequence conservation (**Supplementary Figure 4**) and the reported impact of mutations on RNA binding in *E. coli* TrmA were taken into account (Urbonavičius et al., 2007). Finally, we selected three, conserved and solvent-exposed amino acids on the ß-sheet surface of the RBD (E76A, K104E, F113A) and five in the methyltransferase domain for mutation (K242A, F409A, Q411A, D510A, C538A). This hTRMT2A mutant version was termed Impaired RNA binding (IR) mutant. hTRMT2A IR was used in comparative RNA-binding experiments with hTRMT2A WT, the previously reported catalytic base mutant E581A (CBM), and the catalytic nucleophile mutant C538A (CNM) (Carter et al., 2019) (**Supplementary Figure 1B**). In EMSAs, CBM and CNM mutants showed slightly less binding to $tRNA^{Gln}$ than WT protein when comparing their fractions of unbound RNA at higher protein concentrations (**Figure 4A**). Surprisingly, the IR mutant displayed similar binding as WT, but an increase in supershifted binding events, indicating the difficulties to abolish RNA binding of a protein with a large interaction surface.

Since EMSAs only provide an estimate of binding parameters, we quantified binding affinities of hTRMT2A WT and IR by surface plasmon resonance (SPR) experiments with surface-coupled $tRNA^{Gln}$. In agreement with EMSAs, hTRMT2A WT exhibited high affinity binding with a K_D of 56 ± 16 nM and slow on and off-rates. In contrast, hTRMT2A IR showed a 5-6 times lower affinity (K_D of 304 ± 62 nM) and fast on- and off-rates (**Figure 4B, Supplementary Figure 5**). These results indicate that hTRMT2A IR exhibits a weaker and more transient binding to $tRNA^{Gln}$ as compared to hTRMT2A WT. Consistent with this weaker tRNA binding of hTRMT2A IR, its enzymatic activity is strongly reduced (**Figure 4C**).

Further, methylation by hTRMT2A CBM saturated at lower RNA concentrations and a modestly lower K_M of 0.64 ± 0.06 µM when compared to hTRMT2A WT (**Figure 4C**), which is in line with irreversible trapping of RNA and blocking of the catalytic center. The hTRMT2A CNM showed a three times higher K_m, which indicates less efficient methylation. Since hTRMT2A IR showed weaker RNA binding, as well as the strongest reduction of $tRNA^{Gln}$ methylation, we selected this mutant for further cellular studies.

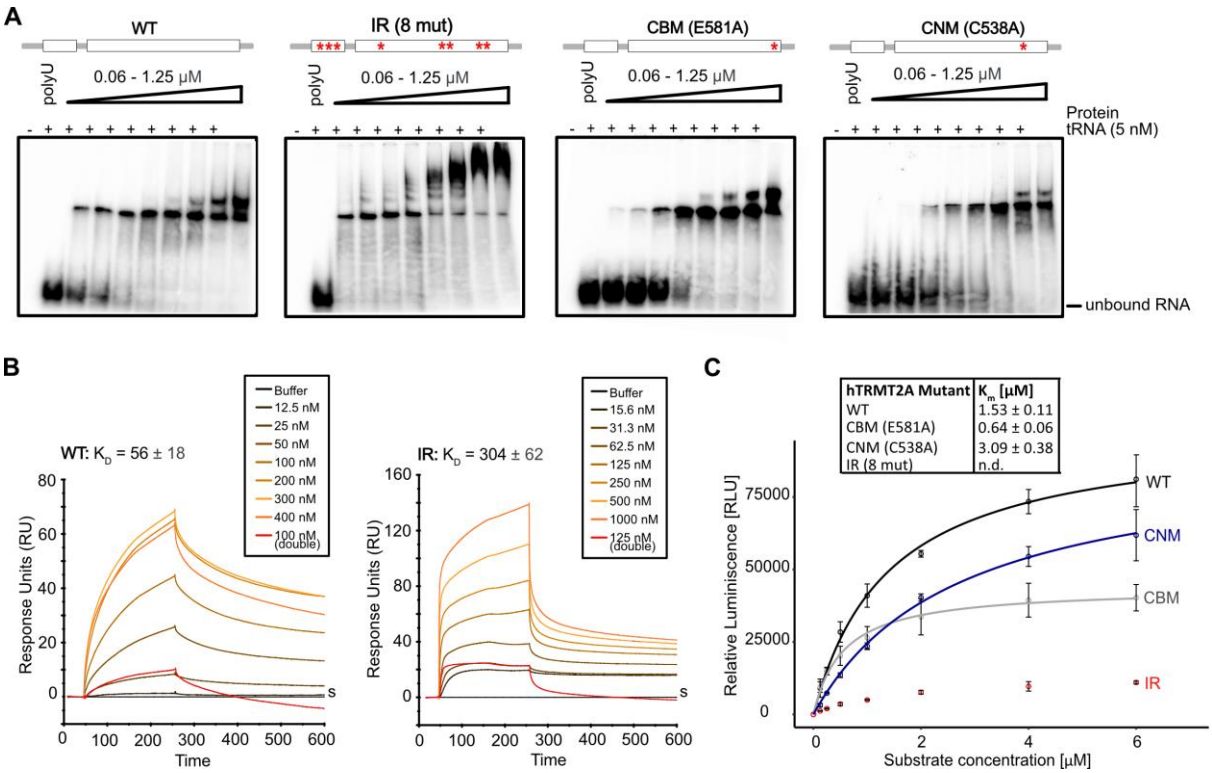

Figure 4 – hTRMT2A IR mutant exhibits reduced RNA binding and impaired enzymatic activity.
A Comparative EMSAs with hTRMT2A WT, IR, CBM and CNM display similar high affinity binding profiles to $tRNA^{Gln}$ in nanomolar K_D range. hTRMT2A IR shows supershifted binding events. Binding assays were performed with ^{32}P labelled $tRNA^{Gln}$. For experiments, polyU competitor and labelled RNA were pre-incubated with increasing concentrations of hTRMT2A for 20 min. Reaction without protein served as control. Free RNA and RNA-protein complex were separated on 4% native PAGE. Each experiment was performed in triplicates. **B** SPR results show a lower K_D for hTRMT2A WT and higher K_D for hTRMT2A IR experiments. For all experiments biotinylated $tRNA^{Gln}$ was coupled to an SA chip. A protein concentration series from 12.5 to 400 nM (WT) and 15.6 to 1000 nM (IR) was injected resulting in the illustrated, double-referenced curves. Representative curves from triplicate measurements are shown. K_D values are from triplicate measurements. **C** K_m curve results for hTRMT2A WT, IR, CBM, CNM mutants from methylation assays confirm strongly reduced enzymatic activity of hTRMT2A IR mutant. For experiments constant protein concentrations and increasing $tRNA^{Gln}$ concentrations were used. Data represent mean ± SD of three replicates. Curves were fitted with Michaelis-Menten equation illustrated as lines. K_m values are listed.

Proximity ligation based interactome of hTRMT2A

To better understand the cellular functions of hTRMT2A, we aimed at an unbiased assessment of its protein interactome and hence its cellular functions by employing proximity dependent biotinylation (BioID) (Roux et al., 2013). In this assay, a protein of interest is fused to the promiscuous biotin ligase BirA* which biotinylates nearby proteins, allowing for the detection of proximal proteins with a distance of up to 10 nm (**Supplementary Figure 6A**). In our study, expression of BirA*-tagged hTRMT2A protein from an overexpression plasmid (**Supplementary Figure 7A**) was induced in biotin supplemented cells. Cells were lysed, biotinylated proteins were captured using streptavidin-beads and analyzed by mass spectrometry (**Supplementary Figure 8A**). To assess the correct sub-cellular localization of the BirA* fusion proteins to nucleus and cytoplasm (Thul Peter J. et al., 2017; Chang et al., 2018, proteinatlas.org), we performed immunostainings against FLAG-tag from the overexpression fusion protein. Immunostainings illustrated that FLAG-tagged hTRMT2A primarily localizes to the nucleus, but also in the cytoplasm**.** These stainings confirm indistinguishable subcellular localization of FLAG-BirA*-tagged, overexpressed hTRMT2A variants (**Supplementary Figure 9**).

BirA* biotinylated many cellular proteins as detected by streptavidin Western blotting (**Supplementary Figure 6B**). The fold change ratios of the mass spectrometry results from WT/BirA* and IR/BirA* were plotted against significance values (**Figure 5A**). After applying cut-off thresholds (Log2 ratio > 2, -Log10 p-value > 3), 222 and 177 proteins were enriched in WT and IR samples over BirA* background control, respectively. Both datasets shared a subset of 115 proteins. Since hTRMT2A IR is impaired in RNA binding, these 115 proteins constitute candidates for potential direct, RNA-independent interactions. GO-term analyses for biological processes and cellular compartments revealed an enrichment of rRNA processing and ribosome biogenesis for protein function and suggested a primary localization of the identified proteins to the nucleolus (**Figure 5B**). These GO terms are consistent with the immunostainings of hTRMT2A (**Supplementary Figure 9**).

Moreover, we compared differences in the interactome of hTRMT2A WT and IR by plotting the hTRMT2A IR/WT ratios against significance levels (**Supplementary Figure 10A**). Notably, proteins that are associated with RNA and nucleic acid metabolic processes were enriched in hTRMT2A WT over IR. This demonstrates that hTRMT2A IR interactors are depleted in nucleic acid associated functions.

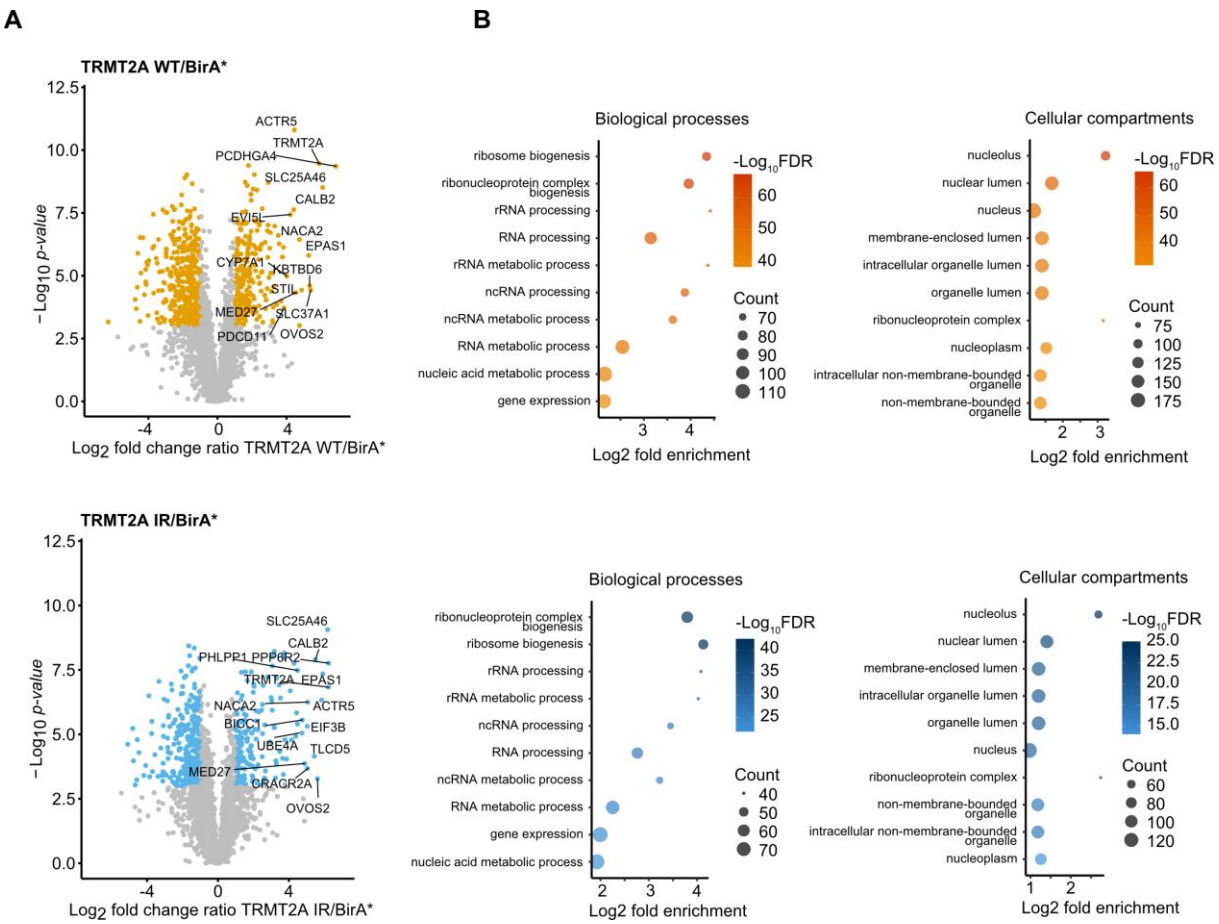

Figure 5 – hTRMT2A WT and IR interactome from BioID experiments.
Volcano plots of hTRMT2A WT (**A**) and hTRMT2A IR BioID (**B**) experiment show enriched proteins and was performed in quintuplicates. Log_2 fold change ratio of hTRMT2A WT (BirA*-tagged)/BirA* background and hTRMT2A IR (BirA*-tagged)/BirA* background was plotted against $-Log_{10}$ p-value. Ratio cut-offs were > 2 and < 0.5 and significance cut-off, with a p-value < 0.05. Hits in agreement with these thresholds are highlighted yellow (WT) and blue (IR), respectively. Top 10 hits are labeled with protein names. Top 10 most enriched GO-terms for biological processes and cellular compartments of hTRMT2A WT (**A**, right panel) and hTRMT2A IR (**B**, right panel) BioID experiments show enrichment of rRNA processing and ribosome biogenesis processes and the nucleolus as most enriched cellular compartment. GO-terms were ranked according to false discovery rate (FDR) as computed with the fisher's exact test. Graphs illustrate GO-terms plotted against Log_2 fold enrichment. Node color represents $-Log_{10}$ FDR. Node size represents counts per GO-term. GO-terms were visualized in R.

Cross-validation of protein hTRMT2A interactors of by co-immunoprecipitation

To cross-validate the interaction partners identified by BioID with a second proteome-wide approach, co-immunoprecipitation experiments (Co-IP) were performed. Co-IP detects protein interactions that are either direct or protein-/RNA-mediated indirect (**Supplementary Figure 11A**). Expression of Flag-tagged hTRMT2A protein and an only Flag-peptide was induced. Cells were lysed, tagged proteins were directly captured using FLAG antibody-coated beads and analyzed by mass-spectrometry (**Supplementary Figure 8B**). Successful elution of FLAG-hTRMT2A and its interacting proteins from beads was confirmed with Western blotting (**Supplementary Figure 11B**). After analysis of the mass spectrometry results, we plotted WT/FLAG and IR/FLAG fold change ratios against significance values (Log2 ratio > 2, -Log10

p-value > 3). This revealed enrichment of 74 and 72 proteins in hTRMT2A WT and IR samples over FLAG background control, respectively (**Figure 6A**). To identify potential RNA-independent hTRMT2A protein interactors, the ratios of significantly enriched proteins from the Co-IP hTRMT2A WT and IR datasets were plotted against each other. Both datasets shared a subset of 39 proteins (**Supplementary Figure 10B**).

The overlap of hTRMT2A WT data from BioID and IP experiments resulted in 13 common proteins, that constitute most confident protein interaction partners (**Figure 6B**). Three of these proteins, SSB (Lupus La protein), TARBP2 and SPINDOC, are additionally enriched in hTRMT2A IR data from BioID and Co-IP experiments. These three common proteins constitute cross-validated, high-confidence candidates for RNA-independent, and likely direct interaction partners of hTRMT2A.

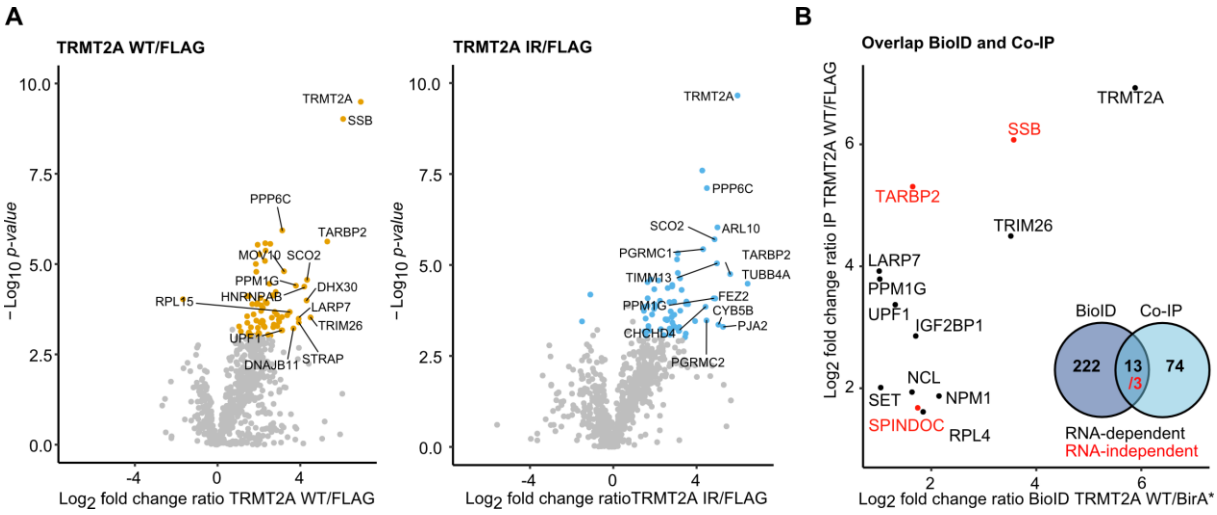

Figure 6 – Potential interaction partners of hTRMT2A.
A Volcano plots of hTRMT2A WT and hTRMT2A IR Co-IP experiment show enriched proteins and was performed in quintuplicates. Log_2 fold change ratio of hTRMT2A WT (FLAG-tagged)/FLAG background and hTRMT2A IR (FLAG-tagged)/FLAG background was plotted against $-Log_{10}$ p-value. Ratio cut-offs were > 2 and < 0.5 and significance cut-off, with a p-value < 0.05. Hits in agreement with these thresholds are highlighted yellow (WT) and blue (IR), respectively. Top 10 hits are labeled with protein names. **B** Overlap of significant hits from hTRMT2A WT BioID and Co-IP data shown as plot of the respective ratios (RNA-dependent interactors = black). Overlap of significant hits from hTRMT2A WT and IR, BioID and IP experiments (RNA-independent interactors = red) shows in the same plot. Venn diagram summarizes overlap of BioID and IP datasets.

hTRMT2A methylates rRNA

The GO-term annotations for biological processes (BioID) and the identification of ribosomal proteins such as RPL4 or NCL as possible hTRMT2A interactors motivated us to explore a potential functional link between hTRMT2A-dependent methylation and rRNA processing/ribosome biogenesis. Previous cryoEM studies of the human ribosomes had revealed all chemical modifications in rRNAs (Natchiar et al., 2017). Two reported sites of m^5U modifications gained our particular interest: m^5U4083 in the 60S subunit and m^5U815 in the 40S subunit. To our knowledge none of these m^5U modifications had been previously associated with a dedicated methyltransferase. Recently, FICC-CLIP experiments confirmed a crosslink of hTRMT2A with the small subunit rRNA (Carter et al., 2019). Moreover, the hTRMT2A homolog hTRMT2B has been shown to methylate tRNA and 12S rRNA in human mitochondria (Powell and Minczuk, 2020). Thus, we hypothesized that hTRMT2A might be the dedicated m^5U methyltransferase of cytosolic rRNA. Two hTRMT2A knockdown HEK293 cell lines (KD1, KD2) were generated using stable transfection of shRNA and were validated previously (Margreiter et al., 2022) (**Supplementary Figure 6B**). For experimental assessment of rRNA methylation status, we isolated cytosolic ribosomes from hTRMT2A WT and KD cells. After rRNA extraction from ribosomes, we verified rRNA purity and its effective separation from tRNA and other RNA species (**Supplementary Figure 12**). Thereafter, rRNA was subjected to mass-spectrometric analysis to investigate whether hTRMT2A is the methyltransferase that catalyzes cytosolic rRNA m^5U conversion. Spiking with a m^5U standard showed sub-stochiometric modification of rRNA in hTRMT2A WT cells in line with around 20 % methylation of one uridine (**Figure 7A**). Analysis of rRNAs in the hTRMT2A KD1 cell line indeed exhibited significantly reduced m^5U levels when compared to WT cells. In contrast, depletion of hTRMT2A in KD2 seemed to have not been sufficient for significant reduction in rRNA methylation. In summary, these findings suggest sub-stoichiometric hTRMT2A-dependent methylation of rRNAs, possibly in positions m^5U4083 in the 60S subunit and/or m^5U815 in the 40S subunit.

hTRMT2A is important for translational fidelity

Previous reports have shown that depletion of certain rRNA modifications can impact ribosome assembly or translation (Schosserer et al., 2015). However, for the hTRMT2A paralog hTRMT2B, a lack of m^5U in rRNA did not affect translation efficiency or mito-ribosome stability (Powell and Minczuk, 2020). Indeed, we have recently shown that in a hTRMT2A deficient situation, protein synthesis is not impaired (Margreiter et al., 2022). This suggests normal ribosome stability and translation efficiency. Therefore, we asked whether translational fidelity might be affected by hTRMT2A KD.

To test this hypothesis, we used a gain of function reporter previously described to detect small increases in mistranslation rates (Javid et al., 2014). The reporter construct contains a fusion protein of renilla and firefly luciferases (derived from *Renilla reniformis* and *Photinus pyralis*, respectively). Single amino acid substitutions within the renilla luciferase (E145Q or D120N) render the enzyme inactive. In a condition with increased translational error rate, the Renilla luciferase would stochastically be synthesized as a functional protein. The dual luciferase setup allowed us to control for protein expression and therefore measure mistranslation accurately.

The reporter constructs were transfected into hTRMT2A WT and KD cells, and luminescence was measured. Indeed, for the E145Q renilla mutation, both KD1 and KD2 cell lines showed significantly increased normalized luminescence ratios, which are in line with an increased mistranslation in hTRMT2A KD over WT. In contrast, no significant increase in mistranslation was observed in the same experiment using the D120N mutation (**Figure 7B**). These observations suggest that E145Q is more prone to mistranslation than D120N.

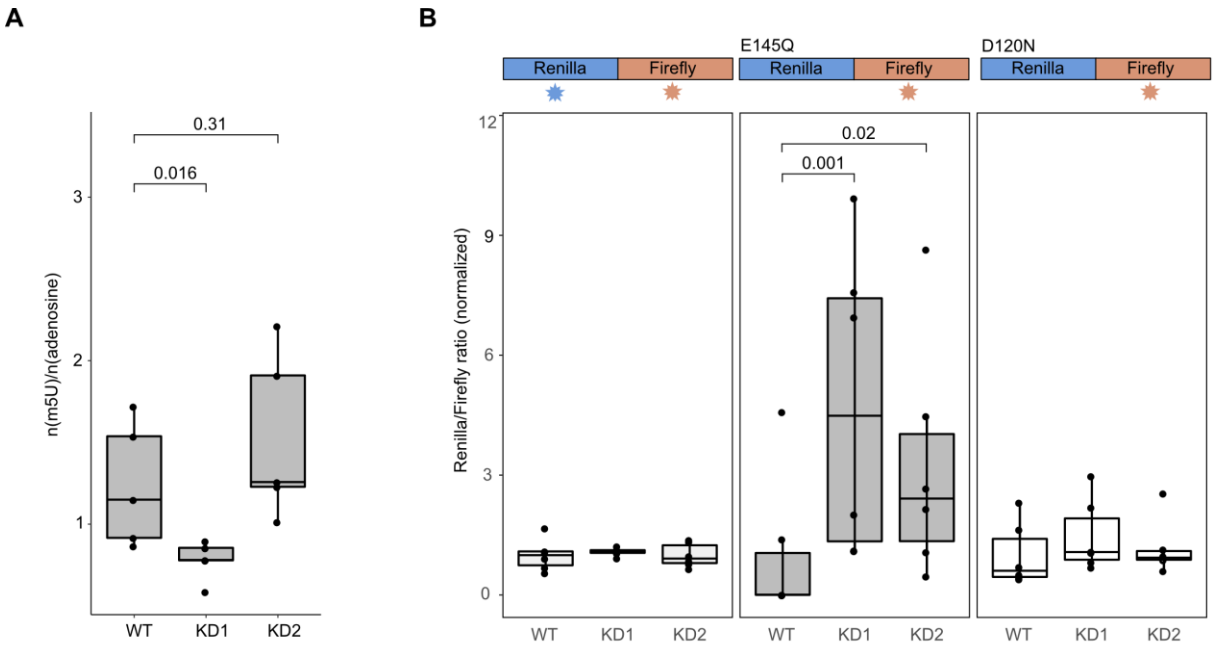

Figure 7 – hTRMT2A impacts rRNA methylation and translational fidelity
A Boxplot of rRNA mass spectrometry analysis. Amount of m^5U was normalized against mass of adenosine and plotted on the y-axis. hTRMT2A KD1 shows significantly decreased rRNA m^5U levels in comparison to WT or KD2. Respective rRNA was obtained from ribosomes that were isolated from WT and two hTRMT2A KD cell lines, KD1 and KD2. Data represents mean ± SD of five biological replicates. Significance was tested with student's t-test with $p > 0.05$ = ns, $p < 0.05$ = significant, p-values are indicated. **B** Translational fidelity assay with dual-luciferase WT, E145Q and D120N mutants and their respective luminescence read-out indicated over the graph. Luciferase plasmids were transfected into hTRMT2A WT, KD1 and KD2. For E145Q luciferase mutant, the ratio in KD1 and KD2 was significantly increased over WT, indicating higher translational error rate. WT and D120N luciferase mutant did not show significant changes. Data represents mean ± SD of six biological replicates in technical triplicates. Significance was tested with Wilcoxon test for non-normally distributed values with $p > 0.05$ = ns, $p < 0.05$ = significant, p-values are indicated.

Discussion

In this study, we characterized the properties of the human tRNA methyltransferase TRMT2A with respect to RNA binding and catalysis. We also identified its RNA-binding interface. Furthermore, we provide the first unbiased assessment of the protein-interaction network of hTRMT2A. These insights suggest novel implications of hTRMT2A and m^5U modification in translation.

hTRMT2A is a promiscuous enzyme that binds target RNAs with low specificity

Previously, it has been shown with FICC-CLIP experiments that hTRMT2A binds to the sequence motif GTTCG(A)A (Carter et al., 2019), which suggests a clear sequence preference of hTRMT2A *in vivo*. In the same study, no further dissection of structural requirements, orthogonal assays or mutational studies of the sequence motif were performed. Thus, we chose positive hits from these experiments to complement available data with our orthogonal *in vitro* experiments. As initial result, we observed that the binding affinity of hTRMT2A for tRNAs was in the expected range. The major parameter that increased methylation efficiency was the presence of a uridine positioned in the T-Loop of the tRNA. However, in our experimental setup binding and methylation was not restricted to tRNA as exemplified by the unrelated *ASH1* E3 stem-loop structured RNA containing a hTRMT2A binding motif (**Figure 1**). In conclusion, our *in vitro* data point towards an enzyme, which binds and methylates not only tRNA, but also other structured RNAs, thus displaying not exclusive preference for tRNA.

Previously, hTRMT2A was analysed in regard to its binding (iCLIP) and methylation (FICC-CLIP) of RNA (Carter et al., 2019). Here, it was apparent that hTRMT2A did not methylate all bound RNA substrates, as exemplified for $tRNA^{Gln\ U54G}$ and $tRNA^{Ala}$ binding and methylation (**Figure 1**). These observations could point in the direction of other, m^5U catalysis-independent functions of hTRMT2A, for example as a tRNA chaperone (Keffer-Wilkes et al., 2020; Schultz and Kothe, 2020).

Apart of the consistent results presented here, we were unable to confirm hTRMT2As interaction with the KCND2 coding region (Carter et al., 2019). In our experimental setting, this RNA was neither bound nor efficiently methylated by hTRMT2A. Potential explanations for this discrepancy include inaccurate *in vitro* RNA folding, missing co-factors for recognition or potentially the higher error rates often occurring in high-throughput experiments. Further experiments will be required to clarify whether KCND2 binding is indeed a physiologically relevant event *in vivo*.

In silico model of hTRMT2A-tRNA^{Gln} complex supported by experimental evidence

So far, there is no complete structure model of hTRMT2As available. Our data from crosslinking experiments followed by mass-spectrometry resolved the hTRMT2A-tRNA^{Gln} interaction surface to a near single amino acid level. To better understand binding of hTRMT2A to tRNA, we used the AlphaFold homology model of hTRMT2A (Jumper et al., 2021) removed protein areas with low confidence prediction scores (< 70 pLDDT, https://alphafold.ebi.ac.uk/entry/Q8IZ69) and mapped the identified crosslinks onto the model Superposition of this homology model to the crystal structure of TrmA bound to a tRNA T-Loop allowed us to confidently superpose a full tRNA^{Phe} (PDB ID: 4TRA) into the homology model (**Figure 8**). The derived hTRMT2A-tRNA^{Phe} model is consistent with experimental observations presented. For example, all three hTRMT2A domains – RBD, central and methyltransferase domain – are in close contact to the modelled tRNA. Hence, this multi-domain interaction of full tRNA is in full agreement with our EMSA experiments, where tRNA binding by hTRMT2A FL was much stronger than binding by its individual subdomains (**Figure 2**). In addition, observed crosslinks are localized around the catalytic center of the model (**Figure 3, Supplementary Figure 3**) and map to the region into which the tRNA T-Loop is predicted to be inserted for methylation. Importantly, the crosslink of amino acid C463, found in all four datasets, resides near the modeled tRNA T-Loop stem. In our homology model of hTRMT2A the crosslinked C270 is placed between T-Loop and D-Loop of the tRNA to potentially interrupt tertiary interactions and render U54 accessible for methylation, as reported for *E. coli* TrmA (Keffer-Wilkes et al., 2020). Both amino acids are also found crosslinked to a dinucleotide UU, which suggests their proximity to the T-Loop U54-U55 or the D-Loop U18-U19 of tRNA. The crosslink of residue H386, found in three of four datasets, is positioned close to the catalytic center, but further away from the modeled tRNA (**Figure 8A**). Several more residues found in less than 3 datasets such as Y331, W176 and C486 positioned close to the catalytic center can be explained with our model. Other crosslinks would require structural rearrangements to be close enough to the RNA such as C191, C225, C329, K559, C551 and C225. As the RBD is connected via an unstructured linker (aa 148-178) to the methyltransferase domain, positioning the RBD with respect to the RNA bears considerable uncertainty (**Supplementary Figure 13**). However, our cross-linking data indicate that the RBD binds RNA with its ß-sheet surface as well as with the flexible loop regions close to crosslinked H83. To account for these experimental data, the position of the RBD was adjusted manually with respect to tRNA (**Supplementary Figure 13, zoom**). The manually curated orientation of the RBD appears to be suitable to form the crosslinking-data suggested interface and thus stabilize the hTRMT2A-tRNA complex.

Interestingly, our model is also consistent with hTRMT2A's limited substrate selectivity with respect to RNA binding and methylation, because large proportions of the tRNA such as the anticodon stem and loop are not bound by hTRMT2A. Deviations in these structures might be tolerated, which would explain binding of other RNAs than substrate tRNA such as stem-looped structured RNA or rRNA (**Figure 1, Figure 8**).

Despite the very consistent insights that arise from combining our experimental data with an advanced homology model, a full comprehension of the hTRMT2A-tRNA interface would require an experimentally determined high-resolution co-structure.

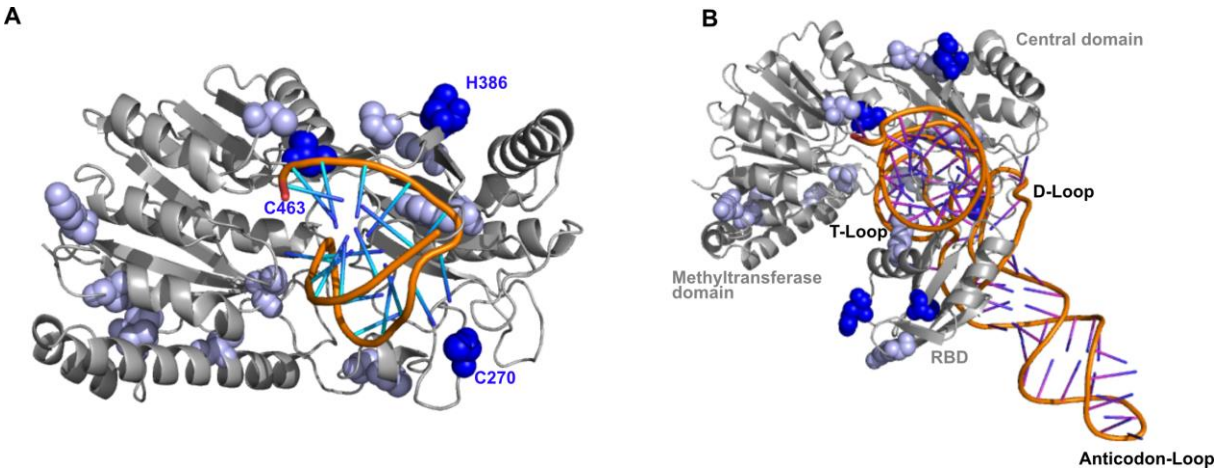

Figure 8 – Model of hTRMT2A-tRNA complex.
A hTRMT2A AlphaFold homology model (grey) overlayed with the T-Loop from *E. coli* TrmA structure (PDB ID: 3BT7; orange). Consistently (blue spheres, 3 of 4 datasets) and less consistently (bright blue spheres, < 3 of 4 datasets) crosslinked amino acids were mapped onto the model. **B** Hybrid model consisting of the hTRMT2A AlphaFold homology model (grey) and an overlayed experimental full tRNA structure (PDB ID: 4TRA) based on the superposition with the *E. coli* TrmA T-Loop co-structure (PDB ID: 3BT7). Crosslinked amino acids from mass spectrometry experiments are highlighted (coloring as in **A**) and mapped onto the hybrid model. Models were generated with PyMOL.

The hTRMT2A interactome and future implications

With BioID and Co-IP we combined the strength of both methods to dissect the hTRMT2A interactome. BioID is superior in recapitulating the physiological nano-scale environment of hTRMT2A, as biotinylation of proteins occurs within intact cells. Moreover, transient interactions can be captured. However, BioID does not allow to distinguish between direct interactors and proximal, non-binding proteins for instance in a very crowded environment such as the nucleolus. In contrast, Co-IP confidently identifies proteins that are part of the same co-complexes including direct and indirect interactions of the bait protein. Moreover, Co-IP also bears the risk of detecting unphysiological interactions that occur only after cell lysis. In particular, for RBPs with lower specificity the risk of false positives is high. Having these differences in mind, we propose that most confident protein interactors can be identified by merging Co-IP and BioID data. A total of thirteen proteins were found both in BioID and Co-IP datasets from hTRMT2A WT cell lines: NCL, TRIM26, hTRMT2A, SSB, TARBP2, LARP7,

PPM1G, UPF1, IGF2BP1, NPM1, SET, SPINDOC and RPL4. Some hits (SSB, TARBP2) were previously identified in orthogonal studies, which may serve as positive controls and indicate that our combinatory interactome study is robust and reliable (Huttlin et al., 2017). Proteins found in BioID and Co-IP from both hTRMT2A WT and IR cell lines were SSB, TARBP2 and SPINDOC, which we propose as most likely RNA-independent protein interaction candidates. Together, these cross-validated candidates indicate biological pathways hTRMT2A likely contributes to. For example, SSB acts as 3' poly(U) terminus dependent transcription factor of RNA polymerase III-dependent transcripts by facilitating proper folding and maturation of target RNA. The best-studied function of SSB is its association with the pre-tRNA 3' trailer, which supports its proper endonucleolytic cleavage (Wolin and Cedervall, 2002). In yeast, early occurring tRNA modifications were installed while the pre-tRNA was still associated with the *S. cerevisiae* homolog of SSB (Etcheverry et al., 1979; Maraia and Intine, 2002). Therefore, hTRMT2A could indeed methylate U54 of pre-tRNA, while the RNA is still associated with SSB. In that context, hTRMT2A and SSB might interact directly as inferred from our BioID/Co-IP data. Also, RISC loading complex subunit TARBP2 was highly enriched both in BioID and Co-IP datasets. Interestingly, SSB prevents mischanneling of tRNA fragments into the human microRNA pathway, which might establish a further link between the hTRMT2A, SSB and TARBP2 (Hasler et al., 2016).

Lastly, hTRMT2A might be implicated in rRNA processing. GO-terms for "rRNA processing" and "ribosome biogenesis" were enriched. Related interaction candidates were identified amongst the top BioID and Co-IP hits (**Figure 5**) such as Nucleolin (NCL), which is involved in pre-rRNA transcription and maturation (Turi et al., 2019) or RPL4, which is part of rRNA processing as well as ribosome biogenesis pathways (Pöll et al., 2009). These implications together with the fact that the human ortholog TRMT2B modifies both mt-tRNA and mt-rRNA, motivated us to assess the m^5U status of cytosolic rRNA isolated from hTRMT2A WT and KD. Indeed, rRNA from one hTRMT2A KD showed a significant reduction of m^5U levels compared to WT cells (**Figure 7A**). This proposes hTRMT2A to be the dedicated methyltransferase not only for cytosolic tRNA, but also cytosolic rRNA. Whether both known m^5U modifications in small and large subunit rRNA are introduced by hTRMT2A is unclear at this point.

As no impact of TRMT2A depletion on protein synthesis was observed (Margreiter et al., 2022), we aimed at addressing the question whether reduced m^5U levels impact translational fidelity. Indeed, in a translational fidelity assay we observed increased translational errors in hTRMT2A KD cells over WT using the E145Q renilla variant, but not with a D120N renilla variant (**Figure 7B**). Differential translation error for one type of mutation but not another, indicates a selective loss of fidelity. One possible explanation is a differential bias in tRNA codon abundance of glutamic and aspartic acid in HEK 293 cells (Behrens et al., 2021). In this context it is worth noting that hTRMT2A has been identified in a *Drosophila*

enhancer/suppressor screen as poly-glutamine (polyQ) disease modifier. Reduced levels of hTRMT2A were associated with decreased polyQ aggregates and photoreceptor death (Voßfeldt et al., 2012). While the rescue effect of decreased hTRMT2A levels on polyQ aggregate formation could be recently validated in human cells, the mode of action has remained elusive (Margreiter et al., 2022). Our observation here suggests that increased translational error rates might cause a stochastic exchange of glutamine for instance against glutamate and therefore disruption of long neurotoxic polyQ glutamine (polyQ) stretches. The tremendous impact of polyQ-stretch disruption on polyQ aggregation has been shown earlier (Menon et al., 2013). However, it remains to be proven whether increase in translational error rate is due to hypomethylation of tRNA, rRNA or other cellular processes such as tRF generation (Pereira et al., 2021). As reduction in translational fidelity is only modest and possibly restricted to certain amino acids, it is not surprising that hTRMT2A WT and KD do not show any apparent phenotypic differences in culture. This is in line with observations in yeast, where depletion of the ortholog Trm2 was not correlated with an adverse phenotype (Nordlund et al., 2000).

Together our *in vitro* RNA binding and methylation data and protein-interactome studies contribute to a basic understanding of the underexplored hTRMT2A molecular and cellular function. Next to its major role in tRNA methylation, these data also uncovered a potential secondary role of hTRMT2A in rRNA processing and translation. Furthermore, since TRMT2A has been described as modulator of neurotoxicity in poly-glutamine aggregation disorders (Voßfeldt et al., 2012; Margreiter et al., 2022) , this study might help to establish TRMT2A as target for therapeutic intervention.

Data availability

The mass spectrometry proteomics data have been deposited to the ProteomeXchange Consortium via the PRIDE partner repository with the dataset identifier PXD036538. Reviewer can access the proteomics data via username reviewer_pxd036538@ebi.ac.uk and password BwOA8SwL.

Acknowledgments

We thank the Core Facility Metabolomics and Proteomics (CF-MPC), especially Ann-Christine König for providing expertise, data recording and analyses. Further, we thank Monika Raabe for help with crosslinking and MS, Matthias Heiss for support with the methods section, and Sebastian Iben for help setting up the translation fidelity assay. We thank Irmgard Diepolder and Vera Roman for technical support. D.N. and A.V. receive funding from the BMBF (PolyQure, 16GW0307). H.U. receives funding from Max Planck Society/MPI-NAT. T.C. and M.W. are funded by the Bayerische Forschungsstiftung AZ-1459-20C, the European Research Council (ERC) under the European Union's Horizon 2020 research and innovation programme under grant agreement No 741912 (EpiR) and by the Deutsche Forschungsgemeinschaft (DFG, German Research Foundation)– Project-ID 321812289 – GRK 2338. DN is funded by the Deutsche Forschungsgemeinschaft (DFG, German Research Foundation)– Project-ID INST 40/656-1.

References

Alian, A., Lee, T.T., Griner, S.L., Stroud, R.M., and Finer-Moore, J. (2008). Structure of a TrmA–RNA complex: A consensus RNA fold contributes to substrate selectivity and catalysis in m5U methyltransferases. Proceedings of the National Academy of Sciences 105, 6876-6881. https://doi.org/10.1073/pnas.0802247105.

Behrens, A., Rodschinka, G., and Nedialkova, D.D. (2021). High-resolution quantitative profiling of tRNA abundance and modification status in eukaryotes by mim-tRNAseq. Molecular Cell 81, 1802-1815.e7. https://doi.org/10.1016/j.molcel.2021.01.028.

Belin, S., Hacot, S., Daudignon, L., Therizols, G., Pourpe, S., Mertani, H.C., Rosa-Calatrava, M., and Diaz, J.-J. (2010). Purification of Ribosomes from Human Cell Lines. Current Protocols in Cell Biology 49, 3.40.1-3.40.11. https://doi.org/10.1002/0471143030.cb0340s49.

Boccaletto, P., Machnicka, M.A., Purta, E., Piatkowski, P., Baginski, B., Wirecki, T.K., Crécy-Lagard, V. de, Ross, R., Limbach, P.A., and Kotter, A., et al. (2018). MODOMICS: a database of RNA modification pathways. 2017 update. Nucleic Acids Research 46, D303-D307. https://doi.org/10.1093/nar/gkx1030.

Boo, S.H., and Kim, Y.K. (2020). The emerging role of RNA modifications in the regulation of mRNA stability. Experimental and Molecular Medicine 52, 400-408. https://doi.org/10.1038/s12276-020-0407-z.

Carter, J.-M., Emmett, W., Mozos, I.R., Kotter, A., Helm, M., Ule, J., and Hussain, S. (2019). FICC-Seq: a method for enzyme-specified profiling of methyl-5-uridine in cellular RNA. Nucleic Acids Research. https://doi.org/10.1093/nar/gkz658.

Chang, Y.-H., Nishimura, S., Oishi, H., Kelly, V.P., Kuno, A., and Takahashi, S. (2018). TRMT2A is a novel cell cycle regulator that suppresses cell proliferation. Biochemical and Biophysical Research Communications. https://doi.org/10.1016/j.bbrc.2018.11.104.

Cheng, Q.-Y., Xiong, J., Ma, C.-J., Dai, Y., Ding, J.-H., Liu, F.-L., Yuan, B.-F., and Feng, Y.-Q. (2020). Chemical tagging for sensitive determination of uridine modifications in RNA. Chemical Science 11, 1878-1891. https://doi.org/10.1039/C9SC05094A.

Cléry, A., Blatter, M., and Allain, F.H.T. (2008). RNA recognition motifs: boring? Not quite. Current Opinion in Structural Biology 18, 290-298. https://doi.org/10.1016/j.sbi.2008.04.002.

Cléry, A., Sinha, R., Anczuków, O., Corrionero, A., Moursy, A., Daubner, G.M., Valcárcel, J., Krainer, A.R., and Allain, F.H.T. (2013). Isolated pseudo-RNA-recognition motifs of SR proteins can regulate splicing using a noncanonical mode of RNA recognition. Proceedings of the National Academy of Sciences 110, E2802-E2811. https://doi.org/10.1073/pnas.1303445110.

Dai, W., Li, A., Yu, N.J., Nguyen, T., Leach, R.W., Wühr, M., and Kleiner, R.E. (2021). Activity-based RNA-modifying enzyme probing reveals DUS3L-mediated dihydrouridylation. Nature Chemical Biology. https://doi.org/10.1038/s41589-021-00874-8.

Das, A.S., Alfonzo, J.D., and Accornero, F. (2021). The importance of RNA modifications: From cells to muscle physiology. WIREs RNA n/a, e1700. https://doi.org/10.1002/wrna.1700.

Edelmann, F.T., Niedner, A., and Niessing, D. (2014). Production of pure and functional RNA for in vitro reconstitution experiments. Methods 65, 333-341. https://doi.org/10.1016/j.ymeth.2013.08.034.

Edelmann, F.T., Schlundt, A., Heym, R.G., Jenner, A., Niedner-Boblenz, A., Syed, M.I., Paillart, J.-C., Stehle, R., Janowski, R., and Sattler, M., et al. (2017). Molecular architecture and dynamics of ASH1 mRNA recognition by its mRNA-transport complex. Nature Structural and Molecular Biology 24, 152 EP -. https://doi.org/10.1038/nsmb.3351.

Etcheverry, T., Colby, D., and Guthrie, C. (1979). A precursor to a minor species of yeast tRNASer contains an intervening sequence. Cell 18, 11-26. https://doi.org/10.1016/0092-8674(79)90349-0.

Grosche, A., Hauser, A., Lepper, M.F., Mayo, R., Toerne, C. von, Merl-Pham, J., and Hauck, S.M. (2016). The Proteome of Native Adult Müller Glial Cells From Murine Retina*. Molecular & Cellular Proteomics 15, 462-480. https://doi.org/10.1074/mcp.M115.052183.

Gustafsson, C., and Björk, G.R. (1993). The tRNA-(m5U54)-methyltransferase of Escherichia coli is present in two forms in vivo, one of which is present as bound to tRNA and to a 3'-end fragment of 16 S rRNA. Journal of Biological Chemistry 268, 1326-1331.

Hasler, D., Lehmann, G., Murakawa, Y., Klironomos, F., Jakob, L., Grässer, F.A., Rajewsky, N., Landthaler, M., and Meister, G. (2016). The Lupus Autoantigen La Prevents Mis-channeling of tRNA Fragments into the Human MicroRNA Pathway. Molecular Cell 63, 110-124. https://doi.org/10.1016/j.molcel.2016.05.026.

Hicks, D.G., Janarthanan, B.R., Vardarajan, R., Kulkarni, S.A., Khoury, T., Dim, D., Budd, G.T., Yoder, B.J., Tubbs, R., and Schreeder, M.T., et al. (2010). The expression of TRMT2A, a novel cell cycle regulated protein, identifies a subset of breast cancer patients with HER2 over-expression that are at an increased risk of recurrence. BMC Cancer 10, 108. https://doi.org/10.1186/1471-2407-10-108.

Hsiao, K., Zegzouti, H., and Goueli, S.A. (2016). Methyltransferase-Glo: a universal, bioluminescent and homogenous assay for monitoring all classes of methyltransferases. Epigenomics 8, 321-339. https://doi.org/10.2217/epi.15.113.

Huttlin, E.L., Bruckner, R.J., Paulo, J.A., Cannon, J.R., Ting, L., Baltier, K., Colby, G., Gebreab, F., Gygi, M.P., and Parzen, H., et al. (2017). Architecture of the human interactome defines protein communities and disease networks. Nature 545, 505-509. https://doi.org/10.1038/nature22366.

Javid, B., Sorrentino, F., Toosky, M., Zheng, W., Pinkham, J.T., Jain, N., Pan, M., Deighan, P., and Rubin, E.J. (2014). Mycobacterial mistranslation is necessary and sufficient for rifampicin phenotypic resistance. Proceedings of the National Academy of Sciences 111, 1132-1137. https://doi.org/10.1073/pnas.1317580111.

Johansson, M.J.O., and Byström, A.S. (2002). Dual function of the tRNA(m(5)U54)methyltransferase in tRNA maturation. RNA 8, 324-335.

Jumper, J., Evans, R., Pritzel, A., Green, T., Figurnov, M., Ronneberger, O., Tunyasuvunakool, K., Bates, R., Žídek, A., and Potapenko, A., et al. (2021). Highly accurate protein structure prediction with AlphaFold. Nature 596, 583-589. https://doi.org/10.1038/s41586-021-03819-2.

Keffer-Wilkes, L.C., Soon, E.F., and Kothe, U. (2020). The methyltransferase TrmA facilitates tRNA folding through interaction with its RNA-binding domain. Nucleic Acids Research. https://doi.org/10.1093/nar/gkaa548.

Kramer, K., Sachsenberg, T., Beckmann, B.M., Qamar, S., Boon, K.-L., Hentze, M.W., Kohlbacher, O., and Urlaub, H. (2014). Photo-cross-linking and high-resolution mass spectrometry for assignment of RNA-binding sites in RNA-binding proteins. Nature Methods 11, 1064-1070. https://doi.org/10.1038/nmeth.3092.

Krendl, C., Shaposhnikov, D., Rishko, V., Ori, C., Ziegenhain, C., Sass, S., Simon, L., Müller, N.S., Straub, T., and Brooks, K.E., et al. (2017). GATA2/3-TFAP2A/C transcription factor network couples human pluripotent stem cell differentiation to trophectoderm with repression of pluripotency. Proceedings of the National Academy of Sciences 114, E9579-E9588. https://doi.org/10.1073/pnas.1708341114.

Laptev, I., Shvetsova, E., Levitskii, S., Serebryakova, M., Rubtsova, M., Bogdanov, A., Kamenski, P., Sergiev, P., and Dontsova, O. (2020). Mouse Trmt2B protein is a dual specific

mitochondrial metyltransferase responsible for m(5)U formation in both tRNA and rRNA. RNA Biology 17, 441-450. https://doi.org/10.1080/15476286.2019.1694733.

Li, Z., Michael, I.P., Zhou, D., Nagy, A., and Rini, J.M. (2013). Simple piggyBac transposon-based mammalian cell expression system for inducible protein production. Proceedings of the National Academy of Sciences 110, 5004-5009. https://doi.org/10.1073/pnas.1218620110.

Maraia, R.J., and Intine, R.V. (2002). La protein and its associated small nuclear and nucleolar precursor RNAs. Gene Expression 10, 41-57.

Margreiter, M.A., Witzenberger, M., Wasser, Y., Davydova, E., Janowski, R., Metz, J., Habib, P., Sahnoun, S.E., Sobisch, C., and Poma, B., et al. (2022). Small-molecule modulators of TRMT2A decrease PolyQ aggregation and PolyQ-induced cell death. Computational and Structural Biotechnology Journal 20, 443-458. https://doi.org/10.1016/j.csbj.2021.12.029.

Menon, R.P., Nethisinghe, S., Faggiano, S., Vannocci, T., Rezaei, H., Pemble, S., Sweeney, M.G., Wood, N.W., Davis, M.B., and Pastore, A., et al. (2013). The Role of Interruptions in polyQ in the Pathology of SCA1. PLOS Genetics 9, e1003648. https://doi.org/10.1371/journal.pgen.1003648.

Mi, H., Muruganujan, A., Casagrande, J.T., and Thomas, P.D. (2013). Large-scale gene function analysis with the PANTHER classification system. Nature Protocols 8, 1551-1566. https://doi.org/10.1038/nprot.2013.092.

Natchiar, S.K., Myasnikov, A.G., Kratzat, H., Hazemann, I., and Klaholz, B.P. (2017). Visualization of chemical modifications in the human 80S ribosome structure. Nature 551, 472-477. https://doi.org/10.1038/nature24482.

Nordlund, M.E., Johansson, J.O., Pawel-Rammingen, U. von, and Byström, A.S. (2000). Identification of the TRM2 gene encoding the tRNA(m5U54)methyltransferase of Saccharomyces cerevisiae. RNA 6, 844-860.

Ny, T., and Björk, G.R. (1980). Cloning and restriction mapping of the trmA gene coding for transfer ribonucleic acid (5-methyluridine)-methyltransferase in Escherichia coli K-12. Journal of Bacteriology 142, 371-379. https://doi.org/10.1128/jb.142.2.371-379.1980.

Pan, T. (2018). Modifications and functional genomics of human transfer RNA. Cell Research 28, 395-404. https://doi.org/10.1038/s41422-018-0013-y.

Pereira, M., Ribeiro, D.R., Pinheiro, M.M., Ferreira, M., Kellner, S., and Soares, A.R. (2021). m(5)U54 tRNA Hypomodification by Lack of TRMT2A Drives the Generation of tRNA-Derived Small RNAs. International Journal of Molecular Sciences 22, 2941. https://doi.org/10.3390/ijms22062941.

Persson, B.C., Gustafsson, C., Berg, D.E., and Björk, G.R. (1992). The gene for a tRNA modifying enzyme, m5U54-methyltransferase, is essential for viability in Escherichia coli. Proceedings of the National Academy of Sciences 89, 3995-3998. https://doi.org/10.1073/pnas.89.9.3995.

Pöll, G., Braun, T., Jakovljevic, J., Neueder, A., Jakob, S., Woolford, John L., Jr., Tschochner, H., and Milkereit, P. (2009). rRNA maturation in yeast cells depleted of large ribosomal subunit proteins. PLoS ONE 4, e8249-e8249. https://doi.org/10.1371/journal.pone.0008249.

Powell, C.A., and Minczuk, M. (2020). TRMT2B is responsible for both tRNA and rRNA m5U-methylation in human mitochondria. RNA Biology 17, 451-462. https://doi.org/10.1080/15476286.2020.1712544.

Ranaei-Siadat, E., Fabret, C., Seijo, B., Dardel, F., Grosjean, H., and Nonin-Lecomte, S. (2013). RNA-methyltransferase TrmA is a dual-specific enzyme responsible for C(5)-methylation of uridine in both tmRNA and tRNA. RNA Biology 10, 572-578. https://doi.org/10.4161/rna.24327.

Roundtree, I.A., Evans, M.E., Pan, T., and He, C. (2017). Dynamic RNA Modifications in Gene Expression Regulation. Cell 169, 1187-1200. https://doi.org/10.1016/j.cell.2017.05.045.

Roux, K.J., Kim, D. in, and Burke, B. (2013). BioID: A Screen for Protein-Protein Interactions. Current protocols in protein science 74, 19231–192314. https://doi.org/10.1002/0471140864.ps1923s74.

Schosserer, M., Minois, N., Angerer, T.B., Amring, M., Dellago, H., Harreither, E., Calle-Perez, A., Pircher, A., Gerstl, M.P., and Pfeifenberger, S., et al. (2015). Methylation of ribosomal RNA by NSUN5 is a conserved mechanism modulating organismal lifespan. Nature Communications 6, 6158. https://doi.org/10.1038/ncomms7158.

Schultz, S.K.-L., and Kothe, U. (2020). tRNA elbow modifications affect the tRNA pseudouridine synthase TruB and the methyltransferase TrmA. RNA. https://doi.org/10.1261/rna.075473.120.

Suzuki, T. (2021). The expanding world of tRNA modifications and their disease relevance. Nature Reviews Molecular Cell Biology 22, 375-392. https://doi.org/10.1038/s41580-021-00342-0.

Swinehart, W.E., Henderson, J.C., and Jackman, J.E. (2013). Unexpected expansion of tRNA substrate recognition by the yeast m1G9 methyltransferase Trm10. RNA 19, 1137-1146. https://doi.org/10.1261/rna.039651.113.

Thul Peter J., Ã…kesson Lovisa, Wiking Mikaela, Mahdessian Diana, Geladaki Aikaterini, Ait Blal Hammou, Alm Tove, Asplund Anna, BjÃ¶rk Lars, and Breckels Lisa M., et al. (2017). A subcellular map of the human proteome. Science 356, eaal3321. https://doi.org/10.1126/science.aal3321.

Turi, Z., Lacey, M., Mistrik, M., and Moudry, P. (2019). Impaired ribosome biogenesis: mechanisms and relevance to cancer and aging. Aging 11, 2512-2540. https://doi.org/10.18632/aging.101922.

Urbonavičius, J., Jäger, G., and Björk, G.R. (2007). Amino acid residues of the Escherichia coli tRNA(m(5)U54)methyltransferase (TrmA) critical for stability, covalent binding of tRNA and enzymatic activity. Nucleic Acids Research 35, 3297-3305. https://doi.org/10.1093/nar/gkm205.

Voßfeldt, H., Butzlaff, M., Prüßing, K., Ní Chárthaigh, R.-A., Karsten, P., Lankes, A., Hamm, S., Simons, M., Adryan, B., and Schulz, J.B., et al. (2012). Large-Scale Screen for Modifiers of Ataxin-3-Derived Polyglutamine-Induced Toxicity in Drosophila. PLoS ONE 7, e47452. https://doi.org/10.1371/journal.pone.0047452.

Wolin, S. L., Cedervall, T. (2002). The La Protein. Annual Reviews in Biochemistry 71:375-403.
https:// doi.org/10.1146/annurev.biochem.71.090501.15000

Wiśniewski, J.R., Zougman, A., Nagaraj, N., and Mann, M. (2009). Universal sample preparation method for proteome analysis. Nature Methods 6, 359-362. https://doi.org/10.1038/nmeth.1322.